Accuracy of kinetic equilibrium reconstruction of NSTX and NSTX-U plasmas and its impact on the transport and stability analysis

G. Avdeeva[1]†, K.E. Thome[1], J.W. Berkery[2], S.M. Kaye[2], J. McClenaghan[1], O. Meneghini[1], T. Odstrcil[1] , S.A. Sabbagh[3], S.P. Smith[1], A.D. Turnbull[1]

[1] General Atomics, P.O. Box 85608, San Diego, CA 05608, USA
[2] Princeton Plasma Physics Laboratory, 100 Stellarator Rd, Princeton, NJ 08540, USA
[3] Columbia University, New York, NY 10027, USA

E-mail: avdeevag@fusion.gat.com

Abstract. An accurate magnetohydrodynamic (MHD) equilibrium reconstruction is an essential starting point for stability and transport plasma analysis. This work describes an approach for obtaining kinetic equilibrium reconstructions using the OMFIT framework, which has been applied for the first time to spherical tokamak data from NSTX and NSTX-U. The EFIT equilibrium solver is integrated with experimental data analysis procedures and subsequent TRANSP transport simulations to enhance the accuracy of the reconstruction, in particular at the edge region, by adding constraints on the total pressure and current density profiles, based on the transport code solution. The accuracy of the equilibrium reconstruction depends on the uncertainty and number of constraints, as well as the choice of basis functions to represent the pressure and current density profiles. An improved fidelity of the equilibrium reconstruction is demonstrated by reducing the variability of the magnetic axis and boundary locations from several centimeters for reconstructions based on magnetic and experimental pressure constraints to only several millimeters for kinetic reconstructions based on transport code constraints, when different representations for basis functions were tested. Variability of the safety factor on-axis was reduced ten times in the same sensitivity study. The accuracy of the equilibrium reconstruction and subsequent mapping of experimental kinetic profile data have a significant impact on TGLF and linear CGYRO turbulence simulations, which predict different spectra of unstable modes and turbulent fluxes for cases with different numbers of constraints in the equilibrium reconstruction. Conversely, the stability analysis performed with the GATO code shows plasmas stable to $n = 1$ MHD modes in both equilibria using magnetic and experimental pressure constraints as well as the transport code constrained equilibrium. However, a scan of parameters away from these conditions shows considerable deviation in the threshold of unstable modes between these reconstructions. Therefore, for reliable plasma analysis and use in turbulence and stability calculations, a high fidelity equilibrium reconstruction with accurate kinetic constraints based on transport code solutions is necessary.

Keywords: Equilibrium reconstruction, spherical tokamaks, EFIT, TRANSP, NSTX

†Author to whom any correspondence should be addressed

1. Introduction

A magnetohydrodynamic (MHD) equilibrium reconstruction provides crucial information for transport and stability analysis of fusion plasmas, such as plasma shape, plasma beta, internal current density and pressure profiles. The magnetic topology information is necessary to map experimentally measured quantities from physical machine coordinates to a flux surface coordinate system, which is typically used as a computational grid in numerical codes for fusion plasma simulations [1]. High fidelity equilibrium reconstructions are essential for issues critical for ITER and the next generation of fusion devices. These include determination of the operational and stability limits, especially for high-performance plasma scenarios, efficient real-time plasma control, disruption prediction, and fast-particle dynamics [2–4].

Filament-based models or models based on Luxon and Brown approaches with non-linear parameterization of the plasma current have been used to obtain the equilibrium reconstruction in the past [5]. Nowadays, one of the most widely used approaches to quickly obtain the equilibrium reconstruction is to solve the axisymmetric force balance Grad-Shafranov (GS) equation [6] while minimizing the least-squares errors with the experimental measurements and the imposed constraints. Various codes have been developed for equilibrium reconstructions on different machines. EFIT [7, 8] is one of the commonly used codes on various devices with some machine-specific variations (including EFIT++ and CAKE [9]); some other codes include LRDFIT [10], LIUQE [11], and NICE [12]. Progress on machine learning and artificial intelligence algorithms have motivated development a device independent version of the equilibrium solver based on the EFIT code [13]. Generally, all these equilibrium codes are based on the similar principle of fitting the experimental data provided in the form of constraints and expanding the pressure and current density profiles in terms of linear basis functions to solve the GS equation. This is an iterative process, using the Picard iteration scheme, until the residual between iterations reaches a prescribed tolerance. A variety of diagnostic measurements are used as inputs to EFIT to impose constraints on the equilibrium solution.

The equilibrium reconstruction based solely on external magnetic measurements should provide an estimate of global plasma quantities [7]; however, it does not have a unique way to represent internal pressure and current profiles due to the ill-constrained nature of the problem [8, 14–16]. Without constraints in the internal plasma region, a wide distribution of possible configurations might satisfy the GS equation and equally minimize the deviation between experimental and reconstructed signals for the available magnetic measurements. The accuracy of equilibria in such cases depends strongly on the quality of the measurements and the parameterization of basis functions to represent the pressure and current density profiles. To improve the fidelity of the equilibrium reconstructions, experimental measurements of kinetic plasma profiles (which usually implies the electron and ion plasma density and temperatures that combined give a thermal plasma pressure) are typically used as additional constraints on the internal pressure profile, in conjunction with motional Stark effect (MSE) or polarimetry measurements applied for current density constraints [17]. To further enhance the accuracy of the internal constraints, the equilibrium reconstruction can be advanced by an integration with transport codes to obtain the plasma profiles of quantities which are typically not measured directly, such as the contributions of the fast-ion pressure and bootstrap current to the total pressure and current density.

The approach presented here uses the OMFIT integrated modeling framework [18], which provides a necessary interface for the equilibrium-transport codes' integration, experimental data analysis, numerical code execution, and theory/experiment comparison. The original workflow for the kinetic equilibrium reconstruction has been successfully applied to the analysis of DIII-D data [18] and has recently been adapted to NSTX [19] and NSTX-U [20] specific data storage systems and diagnostic setup. The low aspect ratio of NSTX(-U) leads to reduced space for diagnostic setup, closer proximity of the plasma to the wall, strong flux compression, stronger plasma rotation, large Shafranov shift and a significant fraction of fast ions to thermal ions compared to conventional tokamaks. Modifications of the workflow were necessary due to the low aspect ratio, differences in diagnostics available on NSTX compared to DIII-D, as well as specifics of the measurements, which in certain cases require additional corrections. In particular, when experimental data from low field side and high field side of the tokamak is mapped onto flux coordinates corrections of experimental data, as well as additional constraints to the equilibrium solver are required due to high plasma rotation and strong centrifugal forces. This work utilizes information (in the form of initial input files) obtained from previous studies of equilibrium reconstruction on NSTX [21–23]. It extends this work by allowing additional constraints based on experimental measurements and, for the first time on NSTX, it provides the integration of the EFIT code with the transport code TRANSP [24] to automatically obtain the total pressure and current density profile constraints.

In this paper, the process of kinetic equilibrium reconstruction for NSTX and NSTX-U using the

OMFIT workflow is discussed in detail. Giving a flexibility in choosing some numerical settings or data analysis approaches, solutions obtained with different options are compared. Then the accuracy of results is estimated by the difference between the maximum and minimum values of the solutions obtained with different settings on each step of the workflow. Although the results are demonstrated only on one selected discharge for NSTX and one for NSTX-U, more shots have been analyzed to verify and generalize the stated conclusions. Additionally, the impact of the accuracy of the equilibrium reconstruction on transport and stability analyses is examined in this work.

The paper is organized as follows. Section 2 describes the kinetic equilibrium OMFIT workflow and experimental shots selected to demonstrate the results. Section 3 is devoted to details and results specific for NSTX plasmas. Impact of the accuracy of the equilibrium reconstruction on the transport and stability analysis for NSTX tokamak is discussed in Section 4. Specific changes in the workflow and observations relevant for the NSTX-U tokamak are presented in Section 5. The main results are summarized in the Section 6.

2. OMFIT workflow for NSTX/NSTX-U equilibrium reconstructions and discharge selection

A reliable equilibrium reconstruction requires self-consistency between multiple constraints provided from various diagnostic measurements and numerical models. Changes in the magnetic equilibrium affect the mapping of the kinetic measurements from real space to flux surfaces and subsequently the transport code solution. To ensure consistency of the solution, the kinetic equilibrium reconstruction on NSTX/NSTX-U is obtained through a cyclic workflow illustrated in Fig. 1, which is similar to that described in Ref. [18].

This workflow includes the following steps:

(i) **Initial equilibrium reconstruction.** First, the initial free-boundary equilibrium is obtained with the EFIT code based on the constraints from available diagnostics. The procedure to add various constraints to input files of the equilibrium solver is described in subsection 3.1. This initial geometric information is required for subsequent mapping of experimental data and analysis with the transport code.

(ii) **Plasma profiles analysis.** In the next step, experimental data is fetched and mapped onto the obtained equilibrium. This step also includes all necessary data analysis procedures required to prepare the data to be used as an input for the transport code, such as filtering, averaging, fitting, and interpolation.

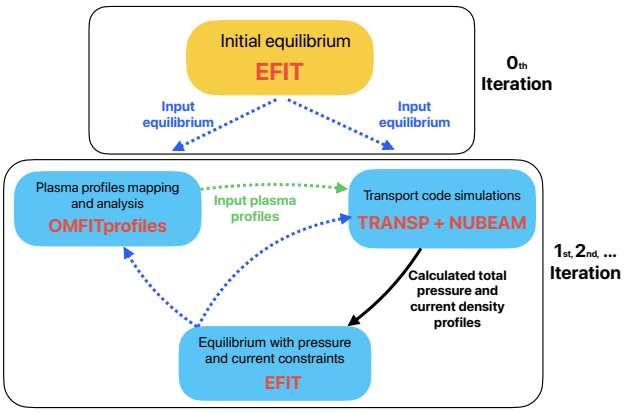

Figure 1. Illustration of the OMFIT workflow for the kinetic equilibrium reconstruction of NSTX/NSTX-U plasmas. The 1st iteration starts from experimental data analysis with OMFITprofiles followed by transport code simulations with input equilibrium and profiles obtained on previous steps.

(iii) **Transport code analysis.** Then, initial equilibrium and plasma profiles are provided as an input to the transport code, which solves the current diffusion equation and includes calculations of the bootstrap current. Transport code analysis also provide information on the neutral beam deposition and the contribution of fast ions to the total pressure.

(iv) **Equilibrium with pressure and current constraints.** When transport analysis is completed, the equilibrium is recalculated using the new total plasma pressure and the new current density profiles for internal constraints.

Several iterations of such a workflow might be required to obtain a self-consistent solution between the equilibrium, experimental profiles mapping and transport code solution. The present workflow can be run step-by-step, if the data quality or a specific analysis requires significant user - data interaction. Alternatively, it can operate in a fully automated mode for large database analysis of similar plasma discharges, where no significant adjustment of numerical settings for each particular case are required. Each step of the workflow will be described in greater detail below with application to NSTX and NSTX-U plasmas.

Fig. 2 presents the time traces of some global quantities for the NSTX and NSTX-U discharges that were selected to illustrate this workflow. The results presented in this paper are obtained for the NSTX H-mode plasma discharge #129017, where equilibria are calculated for multiple time slices between 343 and 595 ms with a time interval of 6 ms. Plasma profiles and magnetic topology shown through the paper

correspond to the time slice 505 ms, when transport and stability analyses are performed. For the NSTX-U representative case, the discharge #204202 is selected and the analysis covers the time interval between 305 and 749 ms with reconstructions performed every 4 ms. The plasma profiles are taken at 550 ms. Both plasma discharges are in a single null divertor plasma configuration and have neutral beam injection (NBI) heating.

The selection of experimental shots is primarily based on the availability of diagnostic data for comprehensive validation studies, and these discharges do not represent the highest plasma parameters or the longest pulse duration achieved on NSTX(-U). The time intervals during the current flat top region are chosen to avoid the plasma current ramp-up and disruption phase of the discharge, where data tend to be of lower quality, resulting in significantly higher uncertainty. Simulating the entire discharge with this OMFIT workflow is possible; however, it might require manual adjustments of the numerical settings for particular time slices. While results are only shown for these two experimental discharges, additional NSTX shots have been analyzed to validate and generalize the findings.

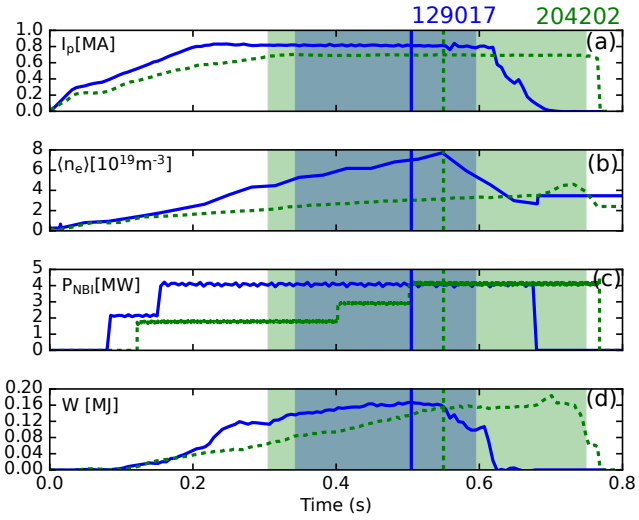

Figure 2. Time traces of (a) plasma current I_p, (b) line-averaged density $\langle n_e \rangle$, (c) NBI injected power P_{NBI} (d) stored energy W for the selected NSTX (solid blue) and NSTX-U (dashed green) discharges. Shaded areas indicate the time intervals, where equilibrium reconstruction is calculated for multiple time slices: green for NSTX and blue for NSTX-U. The vertical lines indicate the time slices from which the plasma profiles shown throughout the paper are taken and stability and transport analysis are also conducted.

3. Equilibrium reconstruction on NSTX

3.1. Initial equilibrium reconstruction

The initial free-boundary equilibrium reconstruction is obtained with the EFIT code. The equilibrium reconstruction process starts with producing input files, which contain imposed constraints provided in the form of diagnostic measurements. The diagnostic uncertainties are used to weigh the data when fitting of experimental data by the equilibrium code is performed.

In this work, the initial input files are collected from the NSTX(-U) data storage system, created according to the MDSplus paradigm [25, 26]. These input files contain the following information, which is not modified in this workflow: a number of magnetic sensors with valid diagnostic data for particular plasma discharge, weight of diagnostic data and correction by wall-induced currents. The latter is significant for the spherical tokamaks even during the current flat top phase [21]. In addition, input files have settings to control the numerical solution of the EFIT code. Typically in this work, the equilibrium is calculated on a 65×65 spatial grid with a maximum of 45 Picard iterations and tolerance below 10^{-3}.

The following subsections are devoted to the description of how various experimental constraints are applied in the initial equilibrium reconstruction of NSTX.

3.1.1. Magnetic constraints. Experimental data from external magnetic measurements is the main constraint to determine the plasma boundary location and global plasma parameters. NSTX has an extensive number of magnetic diagnostics: Mirnov coils and flux loops, located inside and outside the vessel, including the center solenoid and passive plates [21]. Data from up to 43 flux loops and 54 magnetic probes is typically used to provide magnetic constraints together with measurements of the total plasma current by a poloidal Rogowski loop.

In addition to the magnetic diagnostic data, which provide the boundary conditions for the solution of the GS equation, EFIT also requires specifying two functions for the plasma pressure and poloidal current flux, which are typically represented by a polynomial or spline basis set [8, 16, 21]. The most appropriate choice of basis function representation depends on the level of details in the profiles that need to be fitted and errors of the equilibrium solution, which might increase with a higher polynomial order [16, 21]. The polynomial representation of basis functions is typical for the magnetic equilibrium reconstruction, where the shape of internal plasma profiles is unknown. Previous works Ref. [16, 21] have shown that for equilibrium

reconstructions solely based on external constraints, boundary conditions should be set for these basis functions to avoid large values of the high order terms, which could lead to nonphysical solutions.

The accuracy of the solution is usually assessed by χ^2 error, which is a measure of the deviation of experimental signals (M_i) from reconstructed signals computed by EFIT (C_i) and normalized by the measurement uncertainty (σ_i)

$$\chi^2 = \sum_i \left(\frac{M_i - C_i}{\sigma_i} \right)^2 . \quad (1)$$

Another metric, which is called here the GS error, shows the deviation of the solution between neighboring iterations of the EFIT solver as it converges toward the equilibrium solution. A low GS error indicates good convergence of the solution. As observed in this work, high GS errors (> 0.01) are typically associated with nonphysical high values of the safety factor on the magnetic axis.

As the parameterization of current and pressure basis functions is one of the key factors, which might affect the EFIT equilibrium reconstruction, a sensitivity study of the equilibrium reconstruction to the polynomial order of basis functions is performed by independently varying the polynomial order for the pressure and current functions. Equilibrium reconstruction based only on magnetic constraints (Fig. 3) shows that an increase in the polynomial order beyond two for the pressure function results in nonphysical hollow pressure profiles in the plasma core region, or negative pressure at the plasma edge has been seen in reconstructed profiles for some other discharges. It has been observed that although additional constraints applied to basis functions to force $P' = 0$ on the boundary [7, 21] help to get a reasonable converged solution for many cases, it increases the total magnetic χ^2 error.

Results of equilibrium reconstruction based only on magnetic constraints indicate that additional constraints are necessary to obtain physically reasonable converged solutions for both global plasma quantities and internal plasma profiles on NSTX.

3.1.2. Magnetic + experimental kinetic pressure constraints. In addition to the magnetic constraints, the total pressure constraints based on the experimental measurements are applied during the initial equilibrium reconstruction. The electron density n_e and temperature T_e are measured by a Thomson scattering system [27, 28] at 32 spatial locations from the high field side (HFS) to the low field side (LFS) along the plasma mid-plane with a time resolution up to 10 ms. Since major profiles diagnostics including the Thomson scattering system used in equilibrium reconstruction on

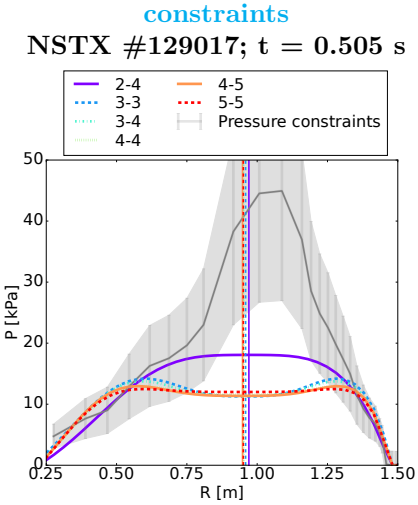

Figure 3. Reconstructed plasma pressure profile in comparison with experimental constraints obtained during variations of polynomials order for pressure (first number in the legend) and poloidal current (second number in the legend) basis functions. Grey area indicates the uncertainty imposed on the pressure constraints, while the solid grey line corresponds to the fitting of experimental data.

NSTX(-U) are located at the tokamak mid-plane, that makes the major radius (R) a convenient coordinate to force the constraints without the requirement to align measurements between different diagnostics.

For simplicity, at this step of initial equilibrium reconstruction it is assumed that the ion and fast-ion pressure are equal to the electron pressure, therefore $P_{total} = P_{electron} + P_{ion} + P_{fastion} = 3 \cdot n_e \cdot T_e$. The ion pressure can be obtained from the charge exchange recombination spectroscopy diagnostic (CHERS) [29]; however, this does not significantly affect the results as large error bars are introduced due to the unknown fast ion pressure. Such assumption is typical for the so called 'partial kinetic' reconstruction when the information of the fast ion pressure is not available as it can not be directly measured [16, 22, 30]. Large error-bars allow flexibility of the reconstructed total pressure profile that provides fast converged solution of the EFIT code, but it also leads to a significant sensitivity of the solution to the basis functions representation as will be shown below. To improve the accuracy of pressure constraints on the next steps of the workflow, calculations of the fast-ion pressure contribution are done with the TRANSP transport code and NUBEAM module [31] and will be discussed in more detail in Section 3.3 where the *full-kinetic* equilibrium is discussed.

The results of the sensitivity study of equilibrium reconstruction to polynomial order of basis functions displayed in Fig. 4 show a noticeable dependency of the magnetic topology on the polynomial order. Variations

of the reconstructed center and boundary positions are in order of several centimeters between different cases that is comparable to the ion gyroradius, which is 9 millimeters near the magnetic axis.

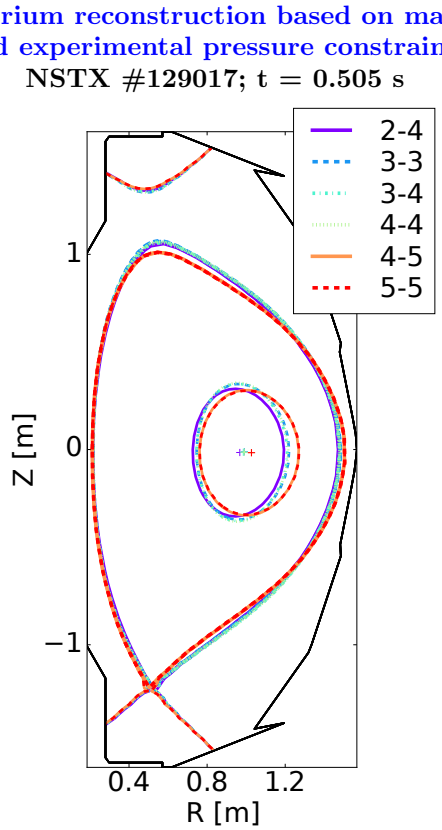

Figure 4. Magnetic topology obtained during variations of the polynomials order for pressure (first number in the legend) and poloidal current (second number in the legend) basis functions .

Plasma profiles are also significantly affected by the variations of the polynomial order. As the polynomial order of both basis functions increases, the plasma profiles become more peaked and the maximum plasma pressure increases (Fig. 5). The comparison of reconstructed profiles with experimental pressure constraints (Fig. 5) indicates that solutions with lower polynomial orders for pressure basis functions underestimate the total pressure in the plasma core region, while solutions with higher polynomial order underestimate the edge pressure.

At the same time, as the polynomial order for both basis functions is above three, the safety factor value on the axis decreases (Fig. 6).

As seen in Fig. 4, 5, 6 variations between solutions diminish as the polynomial order increases, resulting in close solutions between cases with 4th and 5th orders for pressure and current function and the case with 5th order for both functions. Similar trends of increasingly peaked pressure profiles and reduced sensitivity with the rise in polynomial order have been observed in

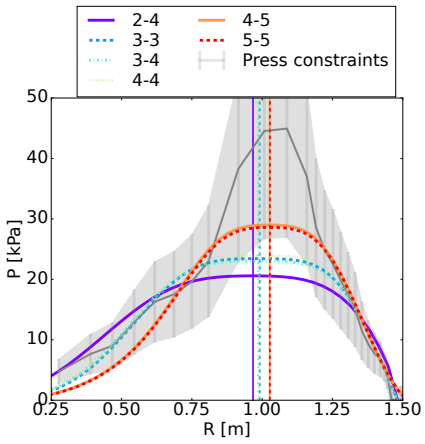

Figure 5. Reconstructed plasma pressure profile in comparison with experimental constraints obtained during variations of polynomials order for pressure (first number in the legend) and poloidal current (second number in the legend) basis functions.

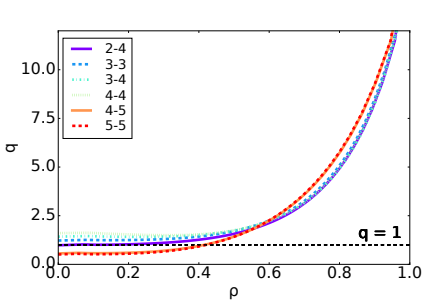

Figure 6. Reconstructed safety factor profiles obtained during variations of polynomials order for pressure (the first number in the legend) and poloidal current (the second number in the legend) basis functions.

other time slices and other NSTX discharges. However, further increase of the polynomial order can lead to overfitting of internal profiles provided with the high uncertainty on this step of the equilibrium. This results in the convergence problems and nonphysical solutions.

As seen in Fig. 7 (a), χ^2 errors are similar across all cases and the GS error (Fig. 7 (b)) is acceptably low in each case. This suggests that the solution of the GS equation with applied constraints is not unique.

Moreover, these error metrics cannot distinguish the fidelity between the obtained solutions. As evident from Fig. 8, a few selected sensors among all the magnetic probes and flux loops used for the equilibrium reconstruction contribute the most to the total χ^2. This trend is observed across several analyzed NSTX

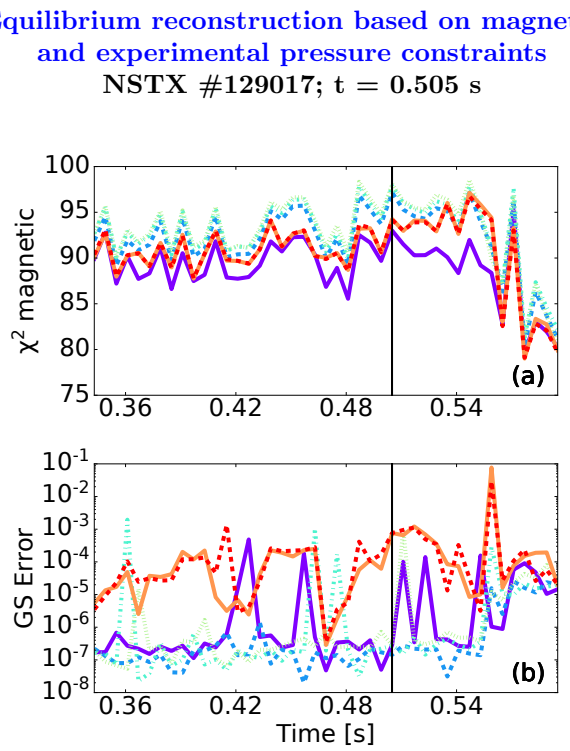

Figure 7. Magnetic χ^2 (a) and GS errors (b) obtained during variations of polynomials order for pressure (first number in the legend) and poloidal current (second number in the legend) basis functions. Legend is the same as in Fig. 4

.

shots. As seen in Fig. 8 (e), signals reconstructed by EFIT for these sensors greatly exceed experimental uncertainty, while for a majority of the magnetic sensors, EFIT provides a solution closely aligned with the given constraints as shown in Fig. 8 (d). A detailed examination of specific issues with selected sensors is outside the scope of this study. Nonetheless, these results highlight the limitations of the total χ^2 error metric for the magnetic equilibrium on NSTX to distinguish between different solutions. A similar trend of consistent χ^2 error levels between cases with different polynomial order has been observed across different shots. Analysis of several NSTX shots revealed that the typical range of the sum of magnetic χ^2 values is approximately 90 - 120. This level is maintained when more constraints are introduced to ensure the consistency among different diagnostic measurements provided to input files. The χ^2 error for the pressure constraints is not estimated and is not discussed on this step of the equilibrium reconstruction due to large error bars of these constraints.

To estimate the sensitivity of the EFIT solution, the difference between the maximum and minimum values of some plasma quantities is calculated for cases obtained during the polynomial order variations. This is done for each time slice and the averaged values are presented in the Table 1, where 'Case 1' corresponds to the magnetic + experimental pressure-constrained equilibrium. As expected, the global plasma quantities (I_p, W_{plasma} defined in the Table 1) are determined quite accurately, while other plasma parameters strongly depend on the order of polynomial basis functions. As seen from the Table 1 the uncertainty of the magnetic axis and boundary location can be several centimeters. Furthermore, the safety factor and maximum pressure can vary significantly and that needs to be taken into account if equilibria with such level of constraints are used for physics analysis.

The equilibrium reconstruction with 4th polynomial order for both basis functions is refereed as *'Mag + Press'* through the rest of the paper.

3.1.3. Magnetic + experimental kinetic pressure + MSE constraints. Additional constraints based on the MSE diagnostic measurements are added alongside with magnetic and experimental kinetic pressure constraints during the initial equilibrium reconstruction on NSTX [32]. This diagnostic measures polarised light emission during a neutral beam injection phase and derives the pitch angle, which is the ratio of toroidal to poloidal components of the magnetic field. Pitch angle equal to zero corresponds to the location of magnetic axis. A 1D radial profile of pitch angle normalized on geometrical coefficients of the diagnostic system are used as a constraint in the plasma equilibrium solver to obtain the toroidal current density distribution [17]. As CHERS and MSE diagnostics have the same radial locations in NSTX, the correction of MSE measurements due to the electric field [33] does not require mapping of experimental rotation profiles; therefore the corrected data is automatically loaded from the data storage server. MSE data points correspond to 11 radial channels, where typically 4 of them are on the HFS and the rest on the LFS and time averaged data over 10 ms is provided as constraints.

Without MSE constraints, the reconstructed polarization angles have a large disagreement with the experimental data (Fig. 9).

By default all constraints, including MSE are applied with the weight equal to one. It has been noticed that for most cases, a higher weight should be imposed to achieve better agreement of reconstructed and experimental data over the entire radial range of experimental points. A change from polynomial to spline representation for the current basis functions does not significantly affect the agreement with experimental data, unless the polynomial order is smaller than 4, then it

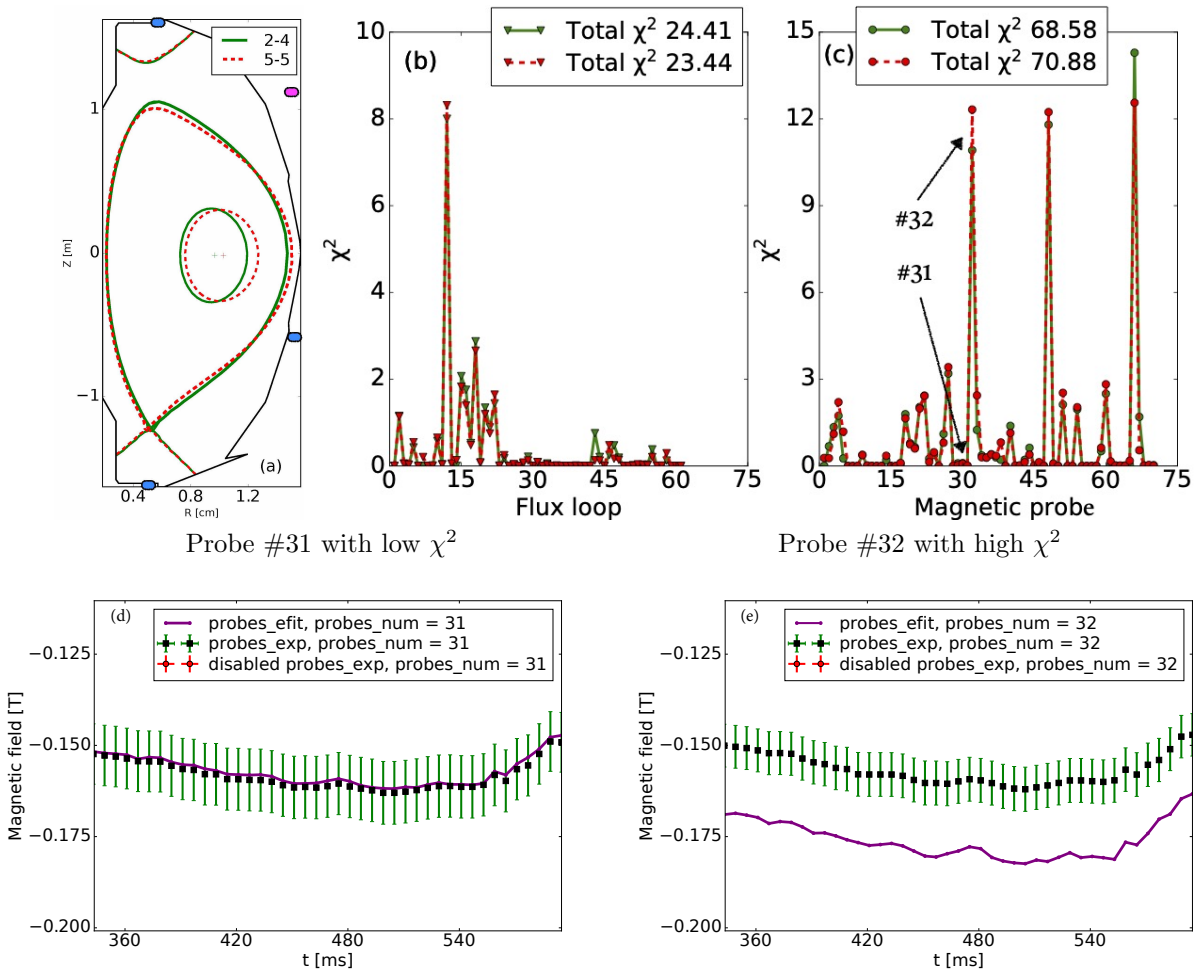

Figure 8. Equilibrium reconstruction based on magnetic and experimental pressure constraints: magnetic topology of two magnetic equilibria obtained with different polynomial order for pressure (first number) and current (second number) basis functions. Blue and pink squares show the location of magnetic probes and the flux loop producing the largest errors (a); χ^2 of each flux loop (b) and each magnetic probe (c); experimental data and EFIT reconstructed signals for probe #31 with low χ^2 (d) and probe #32 with high χ^2 (e).

Symbol	Units	Quantity	Case 1	Case 2	Case 3	Case 4
ΔR_{axis}	[cm]	magnetic axes location	4.4	0.52	0.04	0.25
ΔR_{LCFS}	[cm]	separatrix location at the midplane	2.2	0.82	0.71	0.56
ΔI_p	[MA]	total plasma current	0.01	0.01	0.02	< 0.01
Δl_i		inductance	0.19	0.06	0.05	0.02
ΔW_{plasma}	[MJ]	stored energy	0.02	0.01	0.01	< 0.01
Δq_0		safety factor on axis	0.91	0.12	0.09	0.12
ΔP_{max}	[kPa]	maximum pressure	6.2	1.12	1.03	0.51

Table 1. A sensitivity of the equilibrium solution estimates as a difference between maximum and minimum values for some main plasma quantities obtained during the variations of the polynomial order (Case 1 - Case 3 are averaged over 43 time slices and 6 variations of the polynomial order) or tension of spline (Case 4 - 43 time slices and 11 variations of the polynomial order) on different levels of equilibrium reconstruction: Case 1 - magnetic + experimental pressure constraints; Case 2 - magnetic + experimental pressure + MSE constraints; Case 3 - magnetic + experimental pressure + MSE + Isothermal constraints ; Case 4 - full kinetic equilibrium with magnetic + MSE + transport code constraints.

slightly increases the discrepancy of reconstructed and experimental polarization angles. However, removing the boundary conditions for the basis functions (described in the subsection 3.1.1) noticeably reduces

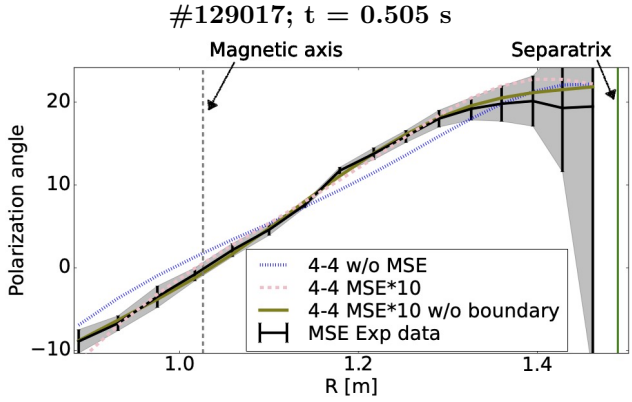

Figure 9. Experimental and reconstructed MSE signals shown for different equilibria: without MSE constraints (w/o MSE), with MSE constraints with weight equal to 10 (MSE × 10). All cases are obtained with 4th order polynomial basis functions and boundary conditions for basis functions are removed in one of the cases (MSE × 10 w/o boundary). $R > 1.4$ corresponds to the pedestal plasma region ($\rho > 0.7$), where errors of MSE measurements increase significantly.

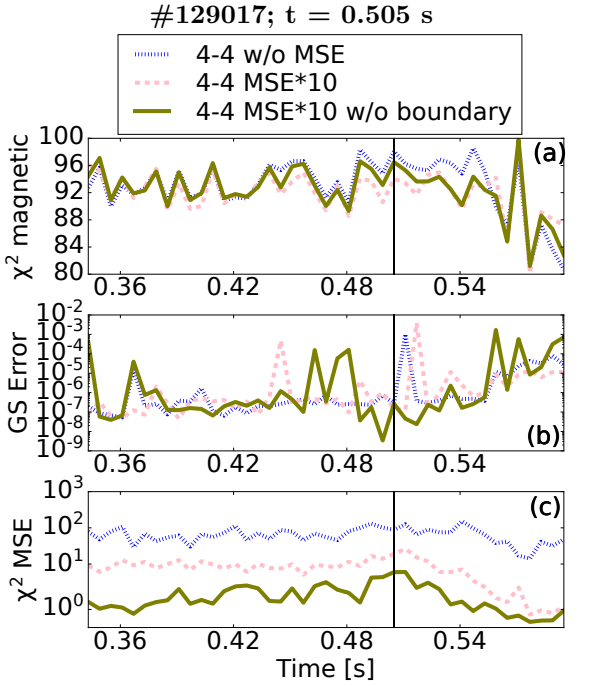

Figure 10. Magnetic χ^2 error (a), GS error (b), MSE χ^2 error (c) shown for different equilibrium: without MSE constraints (w/o MSE), with MSE constraints with weight equal to 10 (MSE × 10). All cases are obtained with 4th order polynomial basis functions and boundary conditions for basis functions are removed in one of the cases (MSE × 10 w/o boundary).

the χ^2 error of MSE data if a high weight on such constraints is imposed (Fig. 9). The equilibrium reconstruction with 4th polynomial order, weight of MSE constraints equal to ten and without boundary conditions for the basis functions is refereed as *'Mag+Press+MSE'* equilibrium.

In all cases, the magnetic χ^2 and GS errors are on the same level, as in the reconstruction with magnetic and pressure constraints (Fig. 10 (a), (b)), indicating consistency between magnetic, kinetic pressure and MSE data provided as constraints to the equilibrium reconstruction.

As seen in Fig. 11, a more peaked pressure profile is obtained with the MSE constraints and the axis location corresponding to the center of the profile is shifted outwards.

The solution of the equilibrium reconstruction with MSE constraints still depends on the order of the polynomial basis functions, but the dependence is noticeably weaker than it was for the equilibrium with the magnetic and kinetic pressure constraints only, as seen in Table 1 (Case 2 versus Case 1). Axis location position as well as the separatrix location became well constrained and the range of variations decreases from several centimeters to millimeters.

MSE measurements provide accurate constraints on the axis location and current density profile in the core plasma region. However, as seen in Fig. 9 the error bars of experimental measurements increase toward the plasma edge and typically these constraints became unreliable at the pedestal plasma region $\rho > 0.7$ (corresponds to $R > 1.4$), where the large bootstrap current contribution should be calculated by numerical models. As both pressure and current functions are terms of the GS equation, the large uncertainty of the pressure constraints affect the current density profile as well, leading to multiple possible solutions even in reconstructions with a high weight of MSE constraints. This is an another reason that more accurate constraints based on the transport code solution should be applied.

3.1.4. Magnetic + experimental kinetic pressure + MSE + Isothermal constraints. One of the modifications of the workflow to NSTX/NSTX-U specific cases is an implementation of additional isothermal constraints, which are possible as the Thomson scattering diagnostic at NSTX has a full radial coverage from LFS to to HFS. Given the assumption of fast parallel heat conductivity, matching electron temperature measurements at two different radii (one at LFS, one at HFS) have to be at the same flux surface. These constraints are implemented by selecting several experimental points on the HFS and then points with

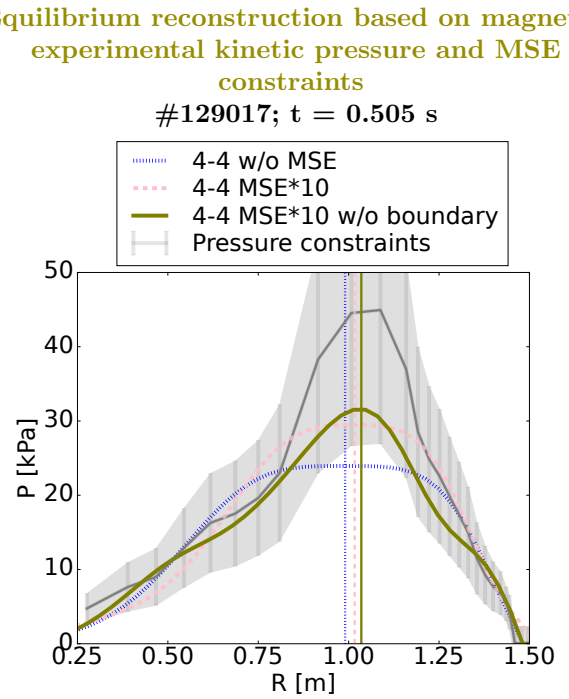

Figure 11. Reconstructed pressure profiles with experimental kinetic pressure constraints shown for different equilibria: without MSE constraints (w/o MSE), with MSE constraints with weight equal to 10 (MSE × 10). All cases are obtained with 4th order polynomial basis functions and boundary conditions for basis functions are removed in one of the cases (MSE × 10 w/o boundary).

the same temperature are found on the LFS, as shown in Fig. 12(a). These pairs of radial locations are provided as constraints into input files and then the equilibrium reconstruction ensures that they are located at the same flux surface. Availability of EFIT to include such constraints is described in Ref. [8].

The number of pairs of radial points is selected automatically based on the defined maximum and minimum temperature thresholds. Depending on the experimental data profile there are typically 3 to 7 points used for the constraints (Fig. 12 (a)). However, the resulting equilibrium negligibly depends on the number and location of these points. The magnetic axis location determining the center of the profile is defined based on the MSE data. It has been observed, that the solution does not converge if isothermal constraints are applied together with MSE constraints with the same weight; this results in a large safety factor profile on the axis. However, a converged solution with a sufficient level of tolerance can be obtained when the weight of the MSE constraint is increased by 10 times. The weight and uncertainty of isothermal constraints is not adjustable; however, ideally the uncertainty in the spatial locations of the diagnostic data should also be considered when constraining the equilibrium reconstruction. The quality of isothermal constraints is verified based on the alignment of experimental measurements on LFS and HFS as demonstrated in Fig. 12 ((b), (c)).

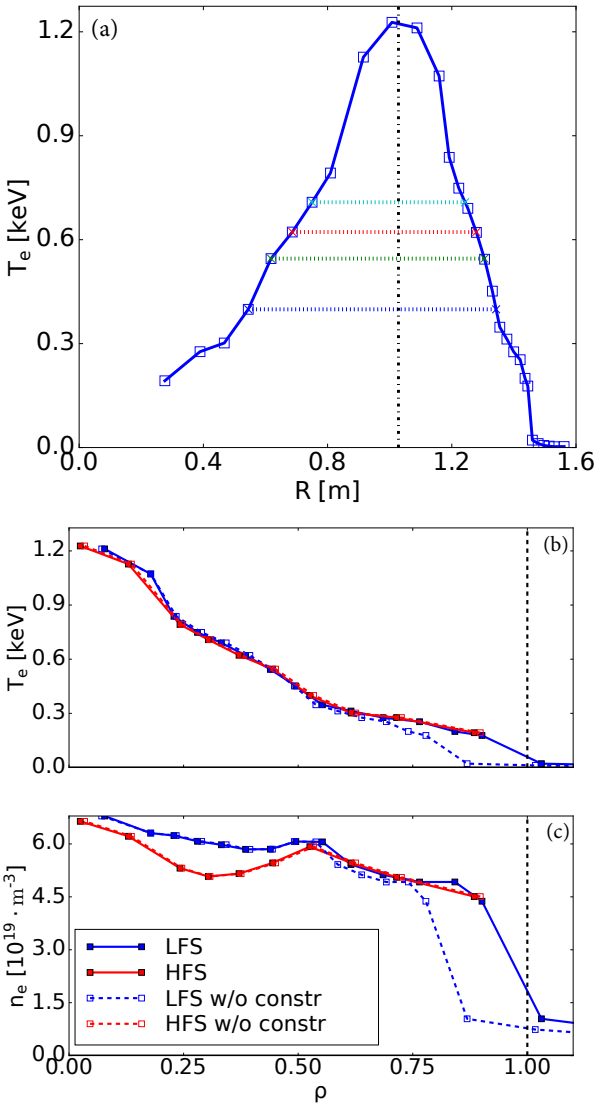

Figure 12. Illustration of the set-up of isothermal constraints (a), electron temperature (b) and electron density (c) Thomson scattering measurements from the LFS and HFS plotted over flux coordinates, obtained during the equilibrium reconstruction with and without isothermal constraints.

The solution with isothermal constraints (Case 3 in the Table 1) weakly depends on the polynomial order of basis functions, compared to other cases. The main reason to apply the isothermal constraints is to require the symmetrization of the electron temperature profile measurements on the LFS and HFS when they are mapped to flux coordinates. However, applying the isothermal constraints leads to a small shift of the plasma boundary inward and an increase

of the magnetic χ^2 error. Further improvement of the accuracy of isothermal constraints would include implementation together with rotation constraints as described in the Ref. [23].

3.2. Analysis of experimental data

The next step in the workflow involves analyzing and mapping the experimental data onto the equilibrium obtained in the previous step. The OMFITprofiles tool [34] is utilized in this workflow for experimental data analysis. This powerful tool has been integrated with the MDSplus data storage server for automated data retrieval. It offers various time convolution windows for data slicing, and incorporates multiple fitting methods and analytical equations to calculate derived quantities such as ion plasma density, effective plasma charge, and the radial electric field, which are necessary inputs for subsequent transport simulations. By employing the OMFITprofiles tool, all experimental measurements and equilibrium reconstructions can be synchronized on the same time frame, enabling the selection of a consistent suite of analysis techniques, including profile fitting methods across different diagnostics and measurements. Utilizing the OMFITprofiles tool within this workflow ensures consistency between equilibrium, experimental data analysis, and power balance calculations.

First, the experimental profiles are mapped to the equilibrium and then convoluted with a window function to the time frame of interest common for all diagnostic measurements [34]. In the current study, the time frame is determined by the available input files for the EFIT code. The convolution window function depends on the time resolution of the diagnostic measurements, and typically it is set between 20 - 40 ms in order to include at least one experimental measurement inside this window. Then, data is fit by one of the fitting methods, and after this such quantities as the ion plasma density or an effective plasma charge can be derived from available experimental data.

Experimental electron temperature and density profiles combine both LFS and HFS measurements. If the equilibrium reconstruction is obtained without isothermal constraints, HFS measurements are neglected, which reduces the number of experimental points by almost half. However, as has been observed in this study, the reduced number of experimental points does not significantly impact the fitting results.

Fast plasma rotation and relatively low ion temperatures on NSTX imply that the deuterium Mach number is near unity, therefore compressibility effects should be considered. As a consequence of particle centrifugal trapping on the LFS of the plasma, an increase of impurity and ion density on this side is observed and a commensurate increase of the electron density to maintain quasi-neutrality of the plasma. To apply a centrifugal force correction to the experimental data, the measured carbon and electron density from the LFS and HFS are recalculated to corresponding flux surface averaged density. This is another addition to the workflow, which has been developed specifically for NSTX/NSTX-U.

The impact of the accuracy of the equilibrium reconstruction on plasma profiles through the mapping of experimental measurements to flux coordinates is demonstrated in Fig. 13. The results present the experimental data mapped on equilibria with different numbers of constraints and then fitted with the spline method. As seen in this figure, mapping on the equilibrium with more constraints leads to higher pedestal plasma parameters at $\rho > 0.8$ (Fig. 13 (a), (b)) due to the shift of experimental points outside, towards the separatrix. This trend is consistent across different time slices and various discharges.

Different fitting methods have been examined to identify which one best represents the shape of the profiles. Additionally, the sensitivity of the subsequent transport code simulations based on these profiles to the choice of the fitting method has been explored and will be shown in Section 3.3. The following fitting methods have been considered: a radial basis function method with different space and time correlation options (labeled as *RBS-6* corresponding to low correlation intervals and *RBS-10* corresponding to higher correlation intervals), a scale length method (*SL-Auto* with automatically defined number of knots and *SL-3* with three knots) and the spline method (*Spline-3* with three knots and *Spline-5* with 5 knots). More details of these fitting methods can be found in Ref. [35]. The same fitting method is used for all experimental measurements in this work, however different methods could be selected for each measurement. Typically, profiles on NSTX have a very wide pedestal structure compared to conventional tokamaks; therefore, fitting methods with hyperbolic tangent function are not considered.

One of the key criteria used to identify the most suitable fitting method of the data analysis is to estimate the deviation of the fitted curve from the actual experimental data points, referred as the residual. However, it is not straightforward to identify the unique best fitting method for all NSTX plasma discharges due to the case-specific nature of many plasma scenarios. For the convenience of quantitative analysis in this work, the residual is calculated as an average over the radial domain and time. It is represented as a percentage from the absolute experimental values. This analysis is performed for experimental data mapped onto equilibria with

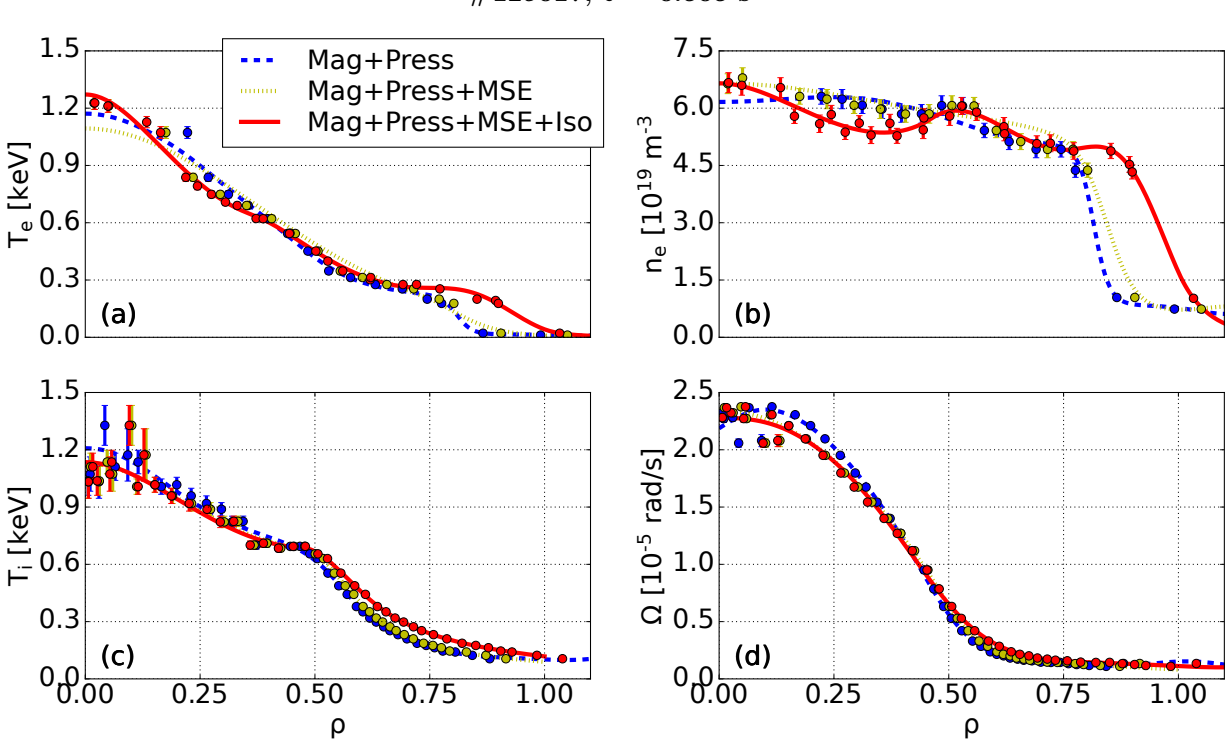

Figure 13. Experimental measurements and fitting of a) electron temperature (T_e), b) electron density n_e, c) ion temperature T_i, d) toroidal rotation Ω profiles obtained with the Spline fitting method. Different colors represent equilibria with varying numbers of constraints, onto which the mapping of experimental points has been performed.

magnetic, pressure, MSE and isothermal constraints. As illustrated in Fig. 14, the distribution trend between maximum and minimum residual values across various fitting methods remains consistent for all experimental measurements. The *Spline-5* and *RBS-10* methods typically result in the lowest residuals across all measured values (Fig. 14), indicating the closest alignment with the shape of experimental profiles. However, these methods can often produce nonphysical spikes, especially in regions with sparse spatial resolution or near the separatrix if no experimental points are available at $\rho > 0.85$.

The scale length fitting method with automatic determination of the number of knots or scale lengths with three knots, along with the spline with three knots, results in the highest residual values among the cases considered (Fig. 14). The *RBS-6* and RBS-10 methods provide quick convergence and high reliability. However, it should be used with caution as it can produce inaccurate results for rapidly changing plasma conditions, particularly when this fitting method uses a substantial correlation time. Similar trends in residual values across various fitting methods have been observed for other shots, though the absolute values of the residual are slightly different. Significantly higher values indicate the fitting method problems and nonphysical solutions described above. In this paper, the *Spline-5* method is primarily used for the analysis, unless specified otherwise. However, in some scenarios, the scale length method proved to be more suitable and convenient.

Figure 15 depicts profiles obtained with various fitting methods, along with experimental points. The choice of fitting method can affect the final values of the plasma profiles to varying degrees, depending on the profile shapes. Due to a non-monotonic structure of some of the experimental profiles there is a noticeable difference observed across the entire radial domain between curves obtained with various fitting methods (Fig. 15 (a), (b)). The discrepancy is more pronounced between methods with a small number of knots, such as *SL-3* and more flexible methods, such as *Spline-5*. The ion temperature and plasma rotation profiles measured by the CHERS diagnostic are generally monotonic and uniform except in the core region. In this area, lower plasma emission leads to increased diagnostic noise, which in turn causes a scattering of experimental data points (Fig. 15 (c), (d).)

To determine and quantify what has a greater impact on the final plasma profiles—the equilibrium reconstruction or the choice of the plasma profile fitting method— the maximum deviation from the reference

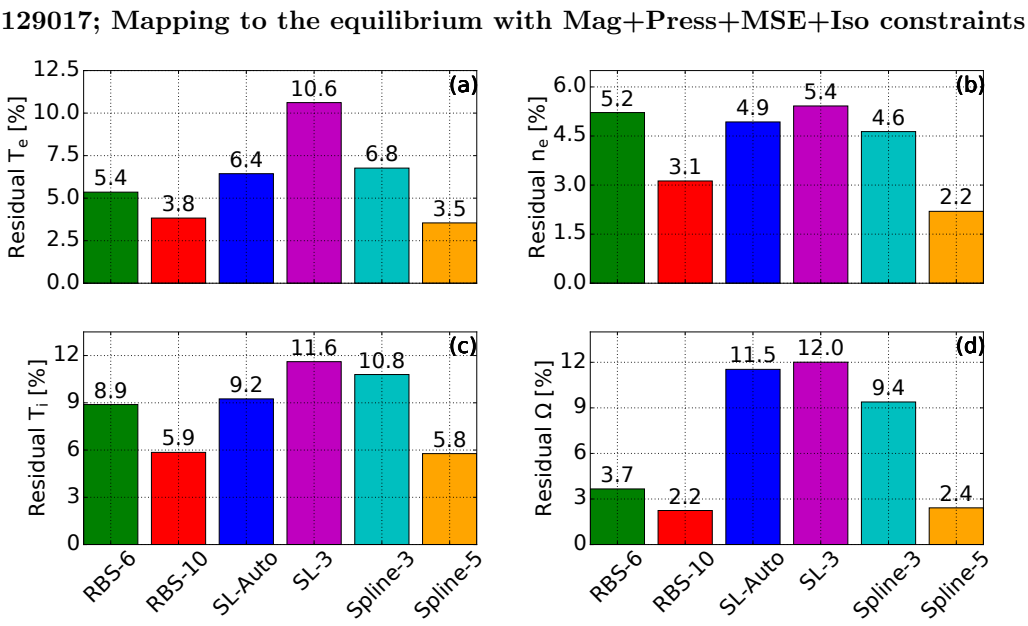

Figure 14. The residual, averaged over time and space, is calculated for different fitting methods. It is measured as a percentage of the absolute experimental values for: (a) electron temperature (T_e), (b) electron density (n_e), (c) ion temperature (T_i), and (d) toroidal plasma rotation (Ω). Data is averaged over 43 time slices and 24 points for T_e, n_e, and 38 points for T_i,Ω.

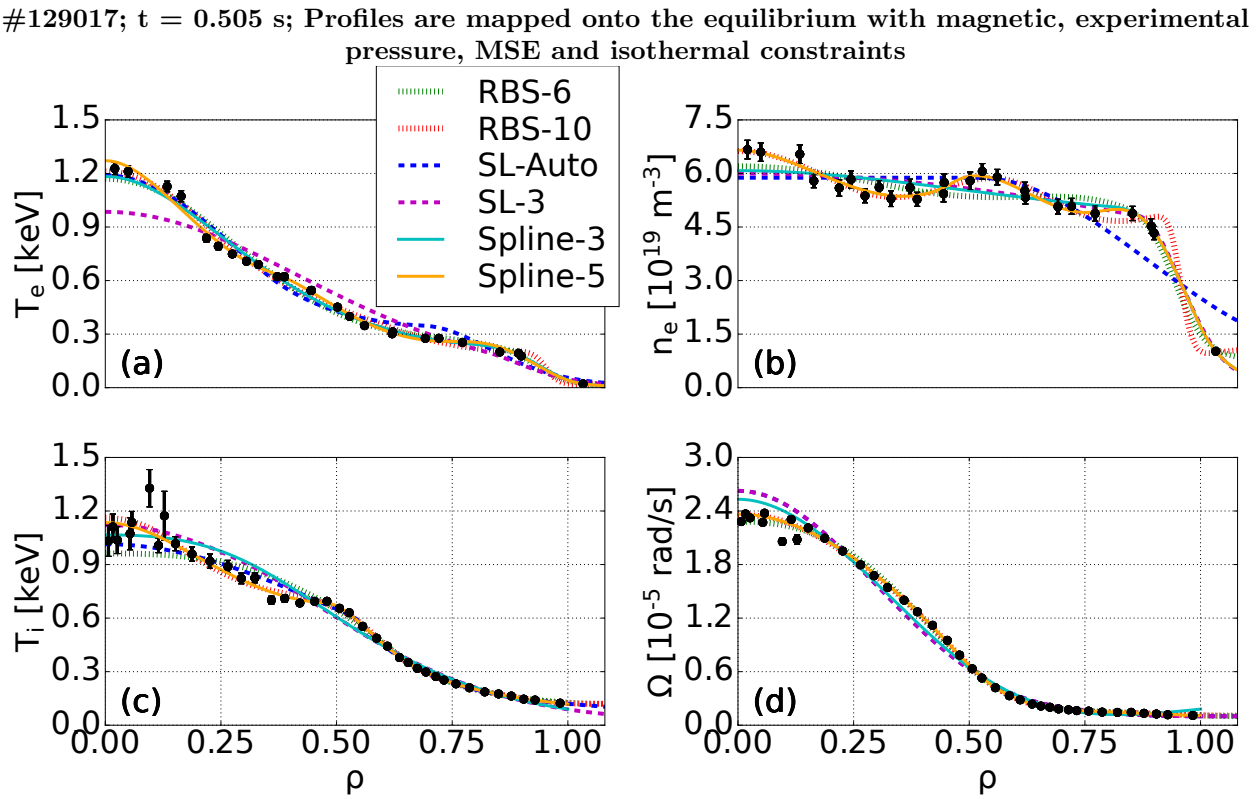

Figure 15. Fitting of experimental measurements a) electron temperature, b) electron density c) ion temperature, d) toroidal rotation obtained with different fitting methods for the shot #129017 at t = 505 ms. The black dots indicate experimental points along with their measurement uncertainties.

case is calculated and then the maximum among different fitting methods is found. This deviation is measured as a percentage of absolute plasma values. The reference case corresponds to the mapping onto the equilibrium with magnetic, pressure, MSE, isothermal constraints and the *Spline-5* fitting method. As depicted in Fig. 16, variations in the equilibrium reconstruction (caused by different numbers of imposed constraints) impact the profile values most significantly at the edge region. Meanwhile, the choice of the fitting method more strongly affects the profiles in the core region within $\rho \leq 0.6$. This trend is observed in other time slices and shots. The mapping to equilibria with various numbers of constraints can result in a 80% change for the electron temperature and up to 70% change for the electron density in the region $\rho =$ [0.7 - 1] (Fig. 16 (a), (b)), which is the most sensitive region for these experimental measurements. However, within the same radial range, the electron temperature and density profiles are nearly half as sensitive to the choice of the fitting method. Depending on the choice of the fitting method, the absolute values of ion temperature and plasma rotation may vary by up to 15% inside $\rho < 0.8$, and more near the separatrix (Fig. 16 (c), (d)). The influence of equilibrium is almost twice as strong for T_i in the region $\rho > 0.5$, but decreases to less than 5% inside the core region (Fig. 16 (c)). Regarding the rotation profile, its sensitivity to both the fitting method and equilibrium mapping is nearly equal at the plasma edge $\rho > 0.5$. However, inside $\rho < 0.5$, the profile shows a higher sensitivity to the fitting method than to the equilibrium mapping (Fig. 16 (d)).

Further in the workflow, the obtained plasma profiles, along with the equilibrium, are used as input for transport code simulations. Therefore, it is crucial to understand and estimate how the accuracy of the equilibrium and sensitivity of experimental profiles to the choice of the fitting method and mapping could propagate as uncertainty and impact the results of the transport code simulations.

3.3. Transport code simulations

Transport code simulations provide total pressure and current density profiles necessary to improve the internal constraints of equilibrium reconstructions. The kinetic plasma profiles are taken from measurements.

3.3.1. Total plasma pressure calculations The fast ions deposition and consequently the contribution of the fast ions to the total plasma pressure are calculated based on the time-dependent power balance analysis with the TRANSP code coupled with the NUBEAM module[31].

The fast-ion pressure resulting from the neutral beam injection is calculated with the NUBEAM code. For NSTX plasmas, the fast ion pressure contribution can be up to 60% of the total plasma pressure on the axis. It decreases towards the plasma edge, becoming negligible at $\rho > 0.6$, as shown in Fig. 17 (a). The fast ion energy makes a substantial contribution to the total plasma energy, typically throughout the entire period of neutral beam injection on NSTX (Fig. 17 (b)).

The comparison of calculated and measured total neutron fluxes is used as a validation of the power balance analysis (Fig. 17 (c)). Due to substantial uncertainly of the absolute calibration of neutron scintillators on NSTX, agreement between calculated and measured values within 30% range is considered as satisfactory in the present analysis. An anomalous fast-ion diffusion can be automatically adjusted by TRANSP to achieve a closer agreement between the calculated and measured neutron fluxes as typically performed in the fast ion plasma transport analysis [36–39]. The anomalous fast ion diffusion coefficients are spatially uniform and typically increase in time as seen in Fig. 18.

The fast-ion pressure depends negligibly on the variations of input parameters generated by mapping of experimental profiles to the equilibrium with various numbers of constraints or various fitting methods. Therefore, the bulk of the discrepancy between the total pressure profiles obtained from TRANSP+NUBEAM simulations with various input files arises from variations in thermal pressure derived from the experimental profiles.

3.3.2. Plasma current density profile calculations TRANSP numerically evolves the poloidal field diffusion equation on a toroidal flux surface grid [40], which allows for obtaining the current density distribution profile. The measured total plasma current or loop voltage are provided in input files as external boundary conditions for the solution. If simulations are set up to match both the current and voltage, the effective plasma charge will be adjusted accordingly, instead of being read from input files, as is typically done when only one boundary condition is applied. The initial conditions are provided through the initialization of a safety factor profile.

The plasma resistivity on each flux surface is calculated from measured plasma parameters based on available analytical models. In TRANSP, the classical resistivity can be obtained by the Spitzer model [41], or neoclassical resistivity can be calculated according to the Sauter [42] model or using the NCLASS [43] module. The bootstrap current can be estimated with either the Sauter or NCLASS models. When the integrated total plasma current is used as a boundary condition, the surface voltage is then calculated from the plasma resistivity and the Ohmic current is

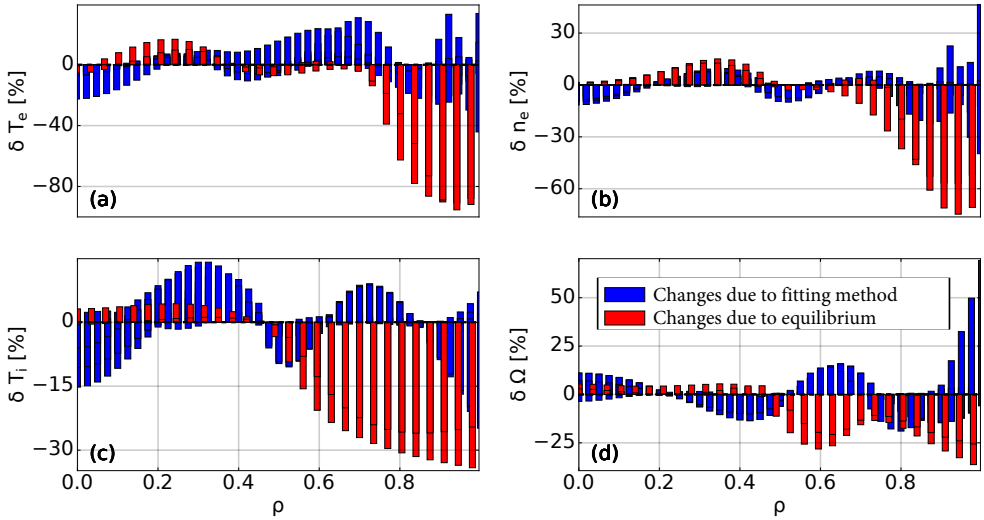

Figure 16. Maximum variations of the plasma profiles, as compared to the reference case ('Spline - 5' Fig. 15), are attributed to differences in the fitting method (which are illustrated in Fig. 15) or the mapping to the different equilibria (which are depicted in Fig. 13).

calculated from the difference between total plasma current and non-inductive contributions: bootstrap current and beam driven current [44].

To illustrate the sensitivity of the current density profiles to the choice of bootstrap model, boundary conditions and variations of input parameters, the different solutions from TRANSP are displayed in Fig. 19. The variations of the boundary conditions for the poloidal field diffusion equation (Fig. 19(a)) indicates that it does not significantly affect the results; however, the calculated current is slightly smaller when only the loop voltage is applied as a boundary condition. It has been found that in other plasma scenarios such a discrepancy can reach approximately up to 20%. The total current density as a boundary condition is generally used in the workflow. As seen in Fig. 19 (b), the solutions with Sauter and NCLASS are very close, while the Spitzer model yields different results inside $\rho < 0.6$. This trend is consistent among different time slices and plasma discharges. Such a discrepancy is expected, as it has been observed that calculations based on classical resistivity are inconsistent with experimental measurements in the plasma core region [45]. The equilibrium reconstruction used for the mapping of experimental profiles, as well as the choice of the fitting method affect the final solution in approximately the same range, and variations of the total current density up to 20% are observed across the entire radial domain (Fig. 19 (c) and (Fig. 19 (d)).

Various contributions to the total current are shown in Fig. 20(a). The beam driven current contribution is substantial only in the core region $\rho \leq 0.5$, where it is comparable with the bootstrap current. In the edge region, the bootstrap current contributes approximately up to 30% of the total current.

As the surface voltage is unconstrained, a comparison of calculated and measured values is used as one of the validation metrics for the solution of the magnetic flux diffusion equation. Another metric is the comparison of MSE experimental signals with a synthetic signal from TRANSP, which can also include correction by the electric field. As seen in Fig. 20(b),(c) both metrics show good agreement between experimental and calculated signals.

3.4. Equilibrium with pressure and current constraints

After the transport code simulations, the obtained total pressure and current density profiles are used as additional constraints in the equilibrium reconstruction, in addition to the MSE and magnetic constraints.

It is well known that the results of the transport code can have uncertainty due to assumptions and simplifications in the models and uncertainty of the data provided in input files. In this workflow, the uncertainty of the pressure profiles is established as 30% of the thermal pressure and 50% of the fast ion pressure, therefore the uncertainty increases toward the plasma core. Despite such a large uncertainty, these pressure constraints are more accurate than the experimental kinetic pressure constraints described in Section 3.1.2.

The current density constraints obtained from the transport code are applied only in the pedestal

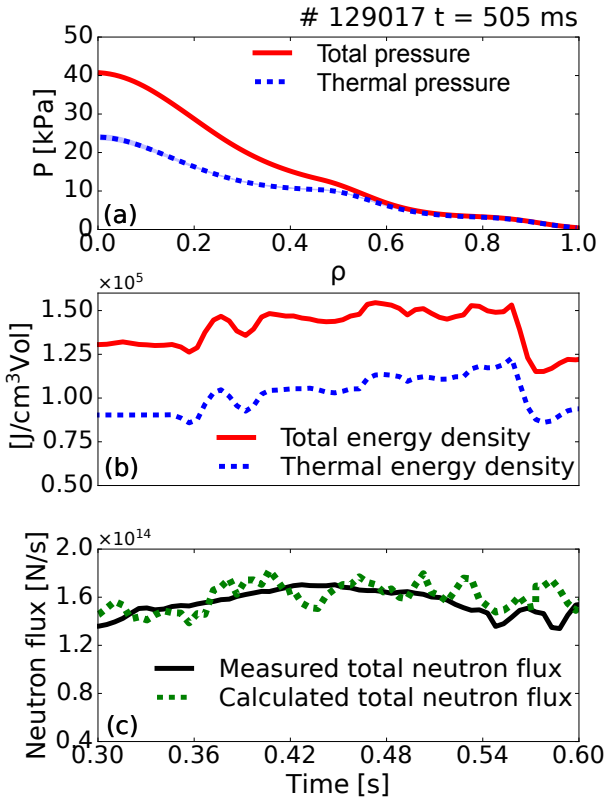

Figure 17. a) The total plasma pressure profile is shown alongside the thermal plasma pressure. b) The total plasma energy density is compared with the fast ion plasma density, displayed as a function of time. Comparison of measured neutron flux with that calculated by TRANSP+NUBEAM displayed as a function of time (c).

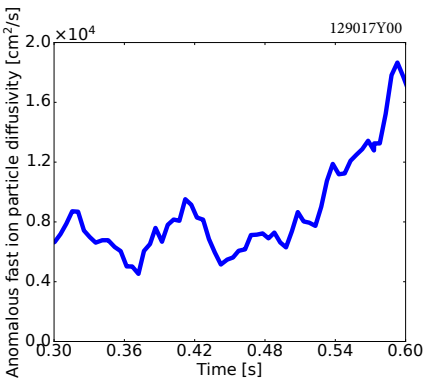

Figure 18. Spatially uniform anomalous fast ion diffusivity automatically adjusted by TRANSP to match the experimental neutron flux, shown as a function of time.

region $\rho > 0.7$, where MSE measurements have large errorbars. The current workflow does not support the uncertainty of the current density constraints, but their rigidity as constraints can be controlled by the weight. It has been found that a weight equal to 1 leads to an increase in both magnetic and MSE χ^2 errors. Therefore, the optimal conditions were found to be to set up the weight equal to 0.1, which is two orders of magnitude lower than MSE constraints and one order of magnitude lower than pressure and magnetic constraints.

For the basis function representation of pressure and current functions, in addition to the polynomial fitting a tension spline representation is available, defined by a set of knot points. While the polynomial representation allows for smooth fitting of profiles, it does not have much freedom to fit to sharp gradients in the pressure and current profiles in the pedestal region. Therefore the spline representation is preferred for the reconstruction with transport code constraints providing accurate pressure and current constraints in the edge plasma region. Five-knot splines are used for both pressure and current basis functions in this work. Increasing the number of knots does not show improvement in the fitting of constraints provided to the equilibrium reconstruction, which would be observed decrease of χ^2 error. Knot locations are adjusted automatically through specifically designed algorithms in OMFIT.

A spline tension defines the way the interpolating function behaves between the knot points. Loose tension provides more freedom to fit the structure of profiles, which is especially important for the accurate reconstruction at the edge pedestal region. On the other hand, without enough regularisation, the fitted profiles can exhibit unphysical oscillations. The default spline tension equal to 1 is used in this analysis, as variations of the spline tension in the range 0.1 - 10 did not show any significant effect on the equilibrium reconstruction.

The final plasma equilibrium, referred to as *'Full kinetic'*, obtained with magnetic, MSE and transport code constraints (total pressure and current density profiles) , is shown in Fig. 21 alongside other solutions with various numbers of constraints.

The boundary location is in a good agreement with magnetic diagnostics as seen from the low magnetic χ^2 in Fig. 22(a), while the GS error is acceptably low Fig. 22(b).

The solution with transport code constraints has significantly higher gradients at the plasma edge and is an exact match of pressure constraints in the edge pedestal region (Fig. 23 (a)). The core current density profile is consistent with the reconstruction based on pressure and MSE constraints, while in the *'Full kinetic'* solution the edge current density profile reflects the increase of the bootstrap current contribution at $\rho \sim 0.8$ (Fig. 23 (c)).

Variations of different settings show that an increase of the pressure on-axis can be obtained only at the cost of realistic current constraints at the

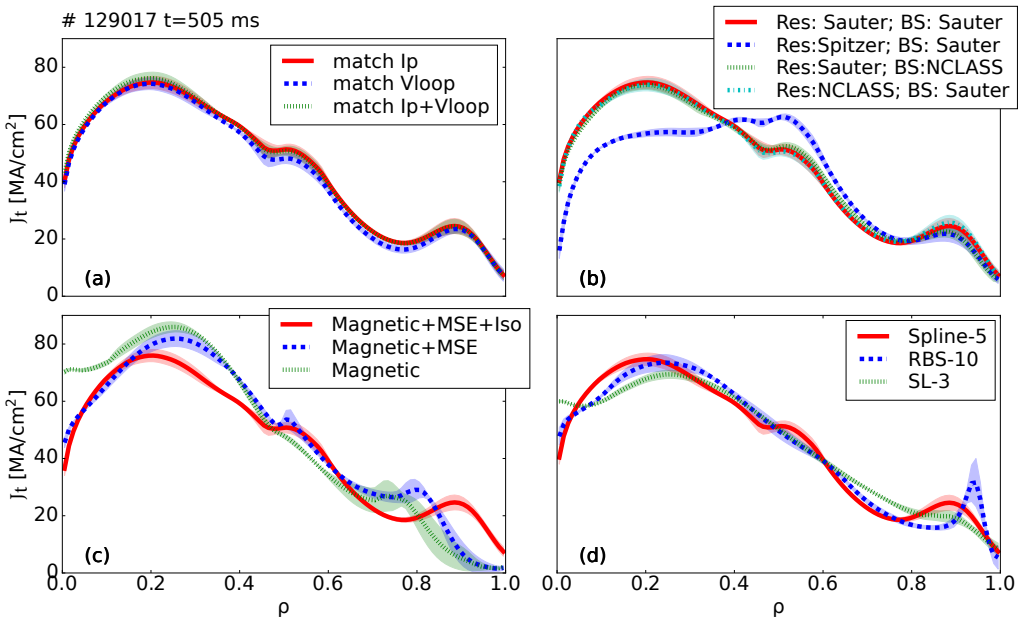

Figure 19. Current profiles obtained by TRANSP+NUBEAM simulations during variations of a) boundary conditions for the poloidal flux diffusion equation, b) resistivity and bootstrap current models, c) equilibrium, and d) fitting method of experimental profiles.

edge, which otherwise would be artificially increased and inconsistent with the current density profiles. Therefore, this solution is defined as optimal even though the total pressure on axis is below the transport code solution, which has large errorbars due to approximations of the used fast-ion model.

The cycle of experimental profiles remapping to the new equilibrium, recalculation of the transport code and equilibrium reconstruction with new constraints has been repeated several times to ensure self-consistency between the experimental profiles, transport code and equilibrium. However, for the discharge considered in this work the difference in the final solution introduced by subsequent iterations is negligibly small.

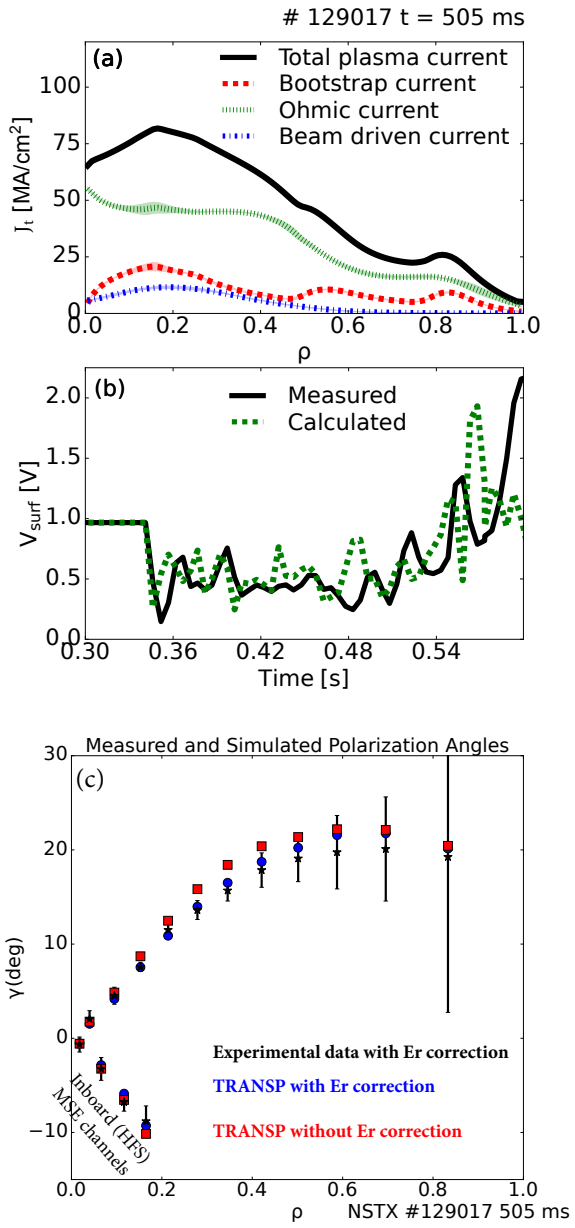

Figure 20. The total plasma current (solid black) density profile is shown alongside with bootstrap (red dashed) , Ohmic (green dotted) and beam driven contributions (blue dashed dotted) (a). The comparison of calculated and measured surface voltage (V_{surf}) shown as a function of time (b). The comparison of MSE experimental signals with synthetic signals calculated by TRANSP with and without correction by the electric field (E_r) plotted over flux surface coordinates (c).

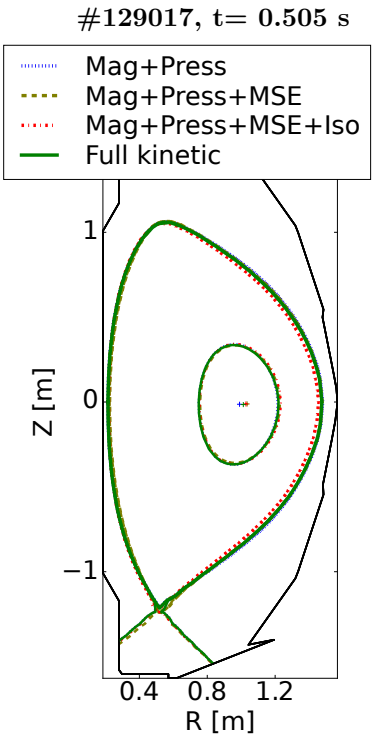

Figure 21. Magnetic topology from reconstructions with various number of constraints.

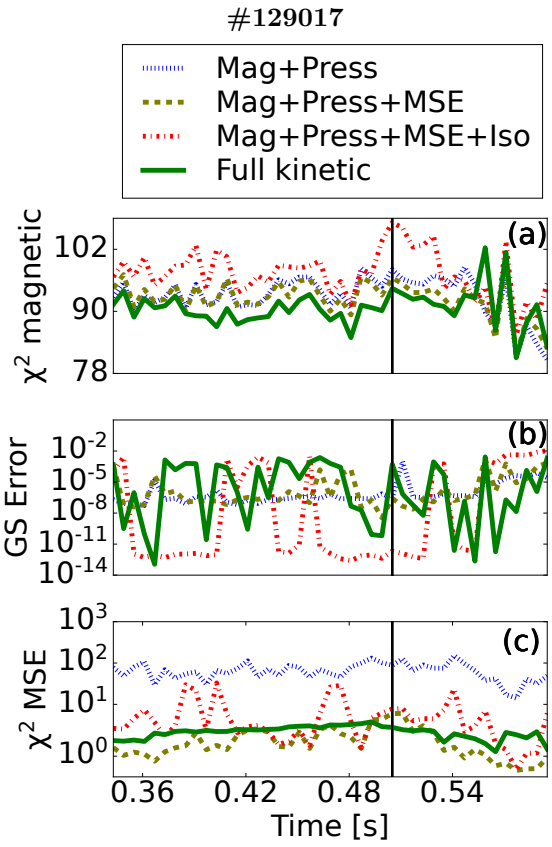

Figure 22. χ^2 error of magnetic diagnostics (a); GS convergence error (b); and χ^2 error of MSE data (c) shown for reconstructions with various number of constraints.

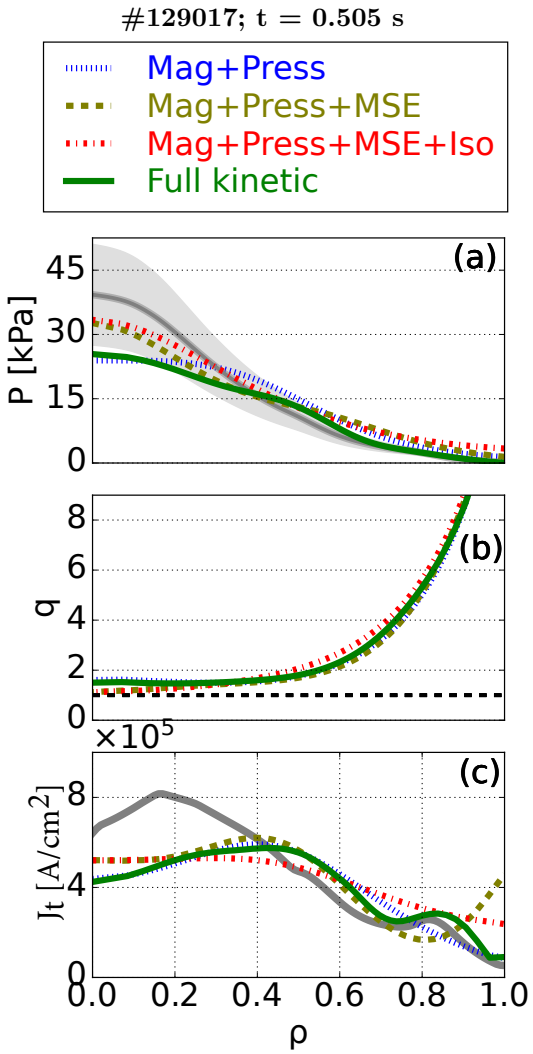

Figure 23. Pressure profile (a), safety factor (b), and current density profiles (c) are plotted over flux coordinates for reconstructions with various number of constraints. Grey curves show pressure and current density profiles obtained from TRANSP simulations. Grey area (a) indicates the uncertainty imposed on the pressure constraints.

4. Effect of the equilibrium on calculations of turbulent transport and MHD stability on NSTX

4.1. Effect of the equilibrium on turbulent transport

The precision of equilibrium reconstruction, along with the mapping of experimental profiles and subsequent power balance analysis, affect outcomes of linear gyrokinetic simulations and turbulence modeling. A series of simulations based on equilibrium (and subsequent experimental data analysis and power balance simulations with TRANSP) with different numbers of constraints is performed with the gyrokinetic code CGYRO [46] and the quasilinear Trapped Gyro Landau Fluid (TGLF) [47] models.

Results of linear CGYRO simulations in the range of low-k (wavenumber) modes performed on different types of input data are presented in Fig. 24 (a),(b). The growth rates (γ) and real frequencies (ω) are in normalized units c_s/a_{unit}, where $c_s = \sqrt{(T_e/m_i)}$ is the ion sound speed and a_{unit} is the outboard midplane minor radius of the separatrix which is used as the unit of length. These simulations do not include electromagnetic effects. Simulations based on the magnetic equilibrium show propagation of unstable modes in the electron diamagnetic direction at $k_\theta \rho_s < 0.8$, where k_θ is the binormal wavenumber and ρ_s is deuterium sound speed over gyrofrequency. The simulations performed on other cases show the propagation of unstable modes in ion diamagnetic direction (Fig. 24 (a)). While growth rates (γ) are above the $E \times B$ shearing rate in all simulations, amplitudes are different between various cases, which is especially pronounced in the region $k_\theta \rho_s \sim 1$. However, similar trends are observed for all solution except one obtained on *Mag+Press* reconstruction.

Equilibrium reconstruction and plasma profiles are connected and are both required as inputs for the CGYRO code. To investigate if either equilibrium or profiles have a bigger effect on the results, simulations with combination of equilibrium and profiles corresponding to Mag+Press and Full kinetic reconstruction are performed and shown in Fig. 25 ((a), (b). As seen from this figure, the results for the same profiles but with different equilibrium are much closer, than results for the same equilibrium but different profiles.

The effect of the equilibrium reconstruction on turbulent transport calculations is assessed with the TGLF reduced transport model. Validation of reduced turbulence models, such as TGLF, on NSTX data has been reported in Ref. [19, 48, 49], where strong sensitivity of predicted plasma profiles based on input parameters has been observed [48]. Total turbulent fluxes measured in GyroBohm normalized

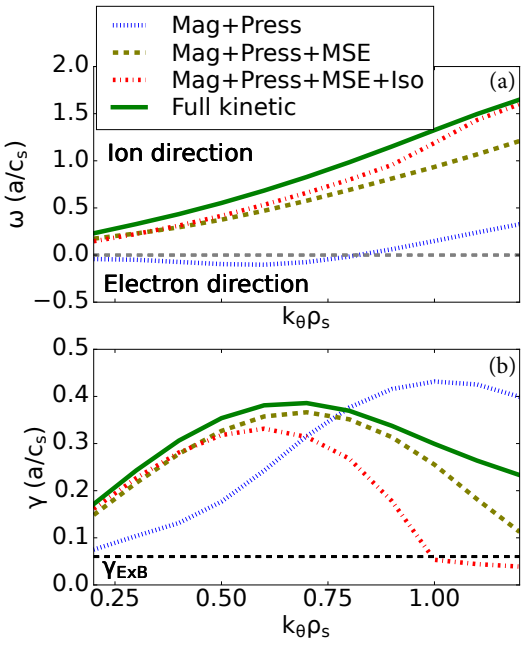

Figure 24. Real frequencies (a) and growth rates (b) obtained from linear CGYRO simulations at ρ=0.7 based on input data obtained on different types of equilibrium. Results are obtained for NSTX #129017; t = 0.505 s

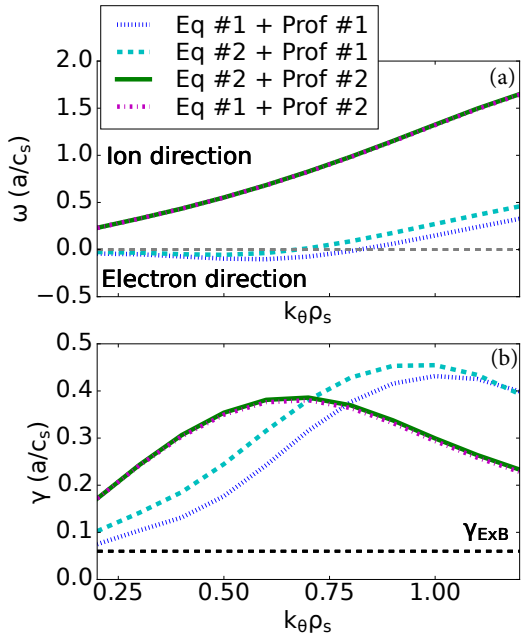

Figure 25. Real frequencies (a) and growth rates (b) obtained from linear CGYRO simulations at ρ=0.7 based on combination of different equilibrium and profiles: Eq #1 and Eq #2 correspond to the reconstructions with Mag+Press constraints and Full kinetic equilibrium respectively; Prof #1 and Prof #2 are plasma profiles obtained by mapping experimental data to Eq #1 and Eq #2. Results are obtained for NSTX #129017; t = 0.505 s

units ($Q_{GB} = n_e T_e c_s (\rho_s/a)$) are shown in Fig. 26 (a), (b). Results obtained for different input files demonstrate sensitivity of the TGLF model to input parameters, which can lead to variations of the output of over an order of magnitude. The spectrum of fluxes (Fig. 26(c), (d)) show that not only is the amplitude of total fluxes different but also the contribution of low and high-k modes to the total fluxes.

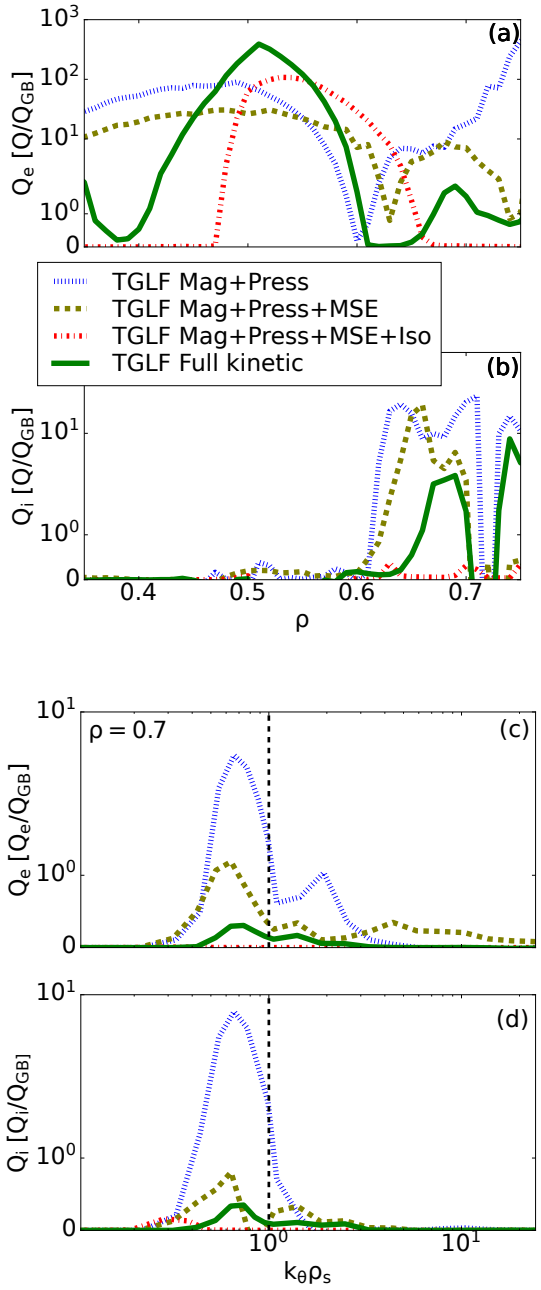

Figure 26. Electron (a) and ion (b) turbulent fluxes calculated by TGLF on inputs corresponding to equilibrium reconstruction with various number of constraints are plotted versus flux coordinates. Spectrum of electron (c) and ion (d) heat fluxes obtained at $\rho = 0.7$ are plotted versus wave-numbers. Results are obtained for NSTX #129017; t = 0.505 s

4.2. Effect of the equilibrium on MHD stability analysis

It is well known that MHD stability analysis can be sensitive to the quality of input equilibria [30, 50, 51]. The stability analysis performed with the GATO code [52] based on equilibrium with magnetic and experimental pressure constraints and full kinetic equilibrium shows stable plasma conditions to $n = 1$ modes in both cases.

To test a sensitivity at the marginal stability conditions, a q_0 scan is performed by resetting the toroidal field to new values, that leave the equilibrium flux surfaces unchanged (but re-scaled) and the poloidal beta fixed [53]. Results show in Fig. 27 indicate that the threshold for unstable modes is different between the magnetic and full kinetic equilibrium. For the lower q_0 case (higher toroidal field), the plasma becomes unstable to a mostly 1/1 mode. Taking into account the large uncertainty of the safety factor on axis for the magnetic plus experimental pressure constrained equilibrium (*Case 0* in Table 1) it is possible that the GATO prediction of the plasma stability can be different for the cases with different order of polynomial basis functions.

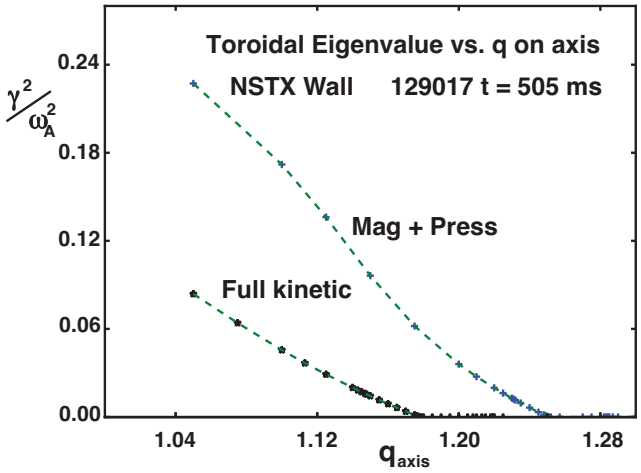

Figure 27. The scan of q_0 demonstrates different thresholds of unstable modes for magnetic plus experimental pressure constraints and full kinetic equilibrium. The vertical axes is the square of the growth rate normalized to a toroidal Alfven time.

For the cases of the magnetic equilibrium with the high order of polynomial basis functions (cases 4-5 and 5-5 Fig. 5, Fig. 6), the plasma is unstable to the internal kink instability since $q_0 < 1$ on the axis (Fig. 28).

5. Equilibrium reconstruction for NSTX-U

The same workflow presented in Fig. 1 and described in Section 3 is used for the reconstruction of equilibria in NSTX-U, the upgraded device. All changes necessary

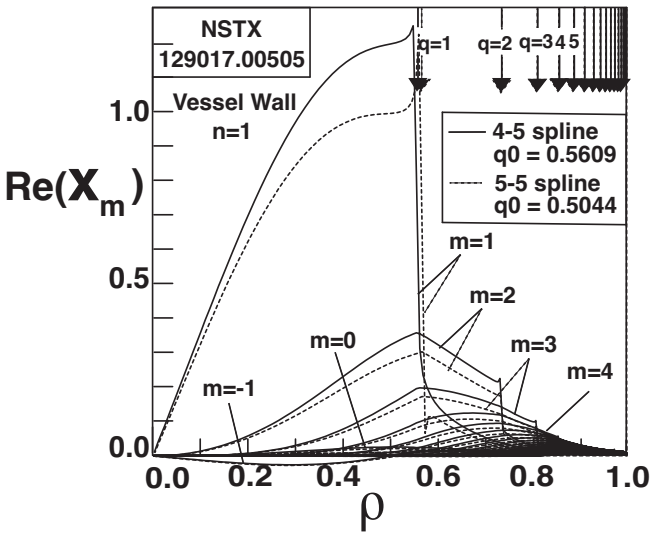

Figure 28. Fourier decomposition of unstable modes in straight field line coordinates obtained with the GATO code for the cases with the high order of polynomial basis functions (cases 4-5 and 5-5 Fig. 5, Fig. 6)

to take into account different diagnostic setup or lack of some data are automatically implemented by the OMFIT workflow, when the device type is changed from NSTX to NSTX-U.

A sensitivity study, similar to that for NSTX described in Section 3, is performed on various steps of the equilibrium reconstruction.

First, the equilibrium based only on the magnetic data is investigated. The overview of the updated set-up of magnetic diagnostics on NSTX-U is presented in Ref. [54]. Experimental data from a larger number of probes and flux loops is applied during the equilibrium reconstruction of NSTX-U compared to NSTX. Therefore, in contrast to NSTX, all solutions are converged with a relatively low level of sensitivity to the polynomial order of basis functions (Table 2 *Case 0*).

The χ^2 error of each magnetic probe and flux loop (Fig. 29) show that there are three probes with significantly larger errors, while the distribution of errors among flux loops is pretty uniform.

On the next step of the analysis, the pressure constraints based on experimental measurements are added and results of the equilibrium reconstruction are presented in Fig. 30, 31, 32 and Table 2 (*Case 1*).

A similar level of magnetic χ^2 and GS errors is demonstrated for all cases of polynomial order variations (Fig. 33 (a), (b)). Similar to the NSTX plasmas, the higher polynomial orders provide steeper and more peaked pressure profiles (Fig. 32).

It should be noted that although the equilibrium reconstruction with pressure constraints shows higher sensitivity to the polynomial order of basis functions (Case 1 versus Case 0 in the Table 2), the total pressure profiles obtained solely on magnetic constraints are much broader and lower compared to that using the kinetic pressure constraints.

The same experimental data analysis and transport code simulation procedure used for NSTX is applied for NSTX-U analysis. Most NSTX-U discharges did not have CHERS and MSE data; however, meaning that the ion temperature, impurity concentration, and plasma rotation profiles were unavailable. In this situation, the workflow automatically skips analysis of these experimental measurements, changes the number of input files provided to the transport code and modifies the settings in the transport code simulations to use a specific model to estimate unknown variables. The ion temperature can be calculated based on the neoclassical ion heat diffusivity and uniform effective plasma charge is assumed in the simplest case.

The pressure and current density profiles are used as additional constraints in the same way as for NSTX, with the only exception that current density profile constraints are applied across the entire radial domain, not only at the edge region. Otherwise many cases do not converge. The comparison of solutions obtained with various number of constraints is shown in Fig. 34, 35, 36. Similar to NSTX, pressure profiles are steeper and in a better agreement with experimental measurements at the edge plasma region when the transport code constraints are applied (*Full kinetic* solution Fig. 36 (a)).

Symbol	Units	Quantity	Case 0	Case 1	Case 2	Case 3
ΔR_{axis}	[cm]	magnetic axes location	1.36	3.39	1.25	0.63
ΔR_{LCFS}	[cm]	separatrix location at the midplane	0.72	1.4	0.27	0.08
ΔI_p	[MA]	total plasma current	0.00	0.01	0.01	< 0.01
Δl_i		inductance	0.12	0.18	0.05	0.01
ΔW_{plasma}	[MJ]	stored energy	0.01	0.02	0.01	< 0.01
Δq_0		safety factor on axis	0.32	0.58	1.02	0.07
ΔP_{max}	[kPa]	maximum pressure	4.62	13.5	4.5	2.19

Table 2. A sensitivity of the equilibrium solution estimated as a difference between maximum and minimum values for some main plasma quantities obtained during the variations of the polynomial order (Case 0 - Case 2) or tension of spline (Case 3) on different levels of equilibrium reconstruction: Case 0 - magnetic; Case 1 - magnetic + experimental pressure; Case 2 - magnetic + experimental pressure + Isothermal constraints; Case 4 - full kinetic equilibrium with magnetic + transport code constraints

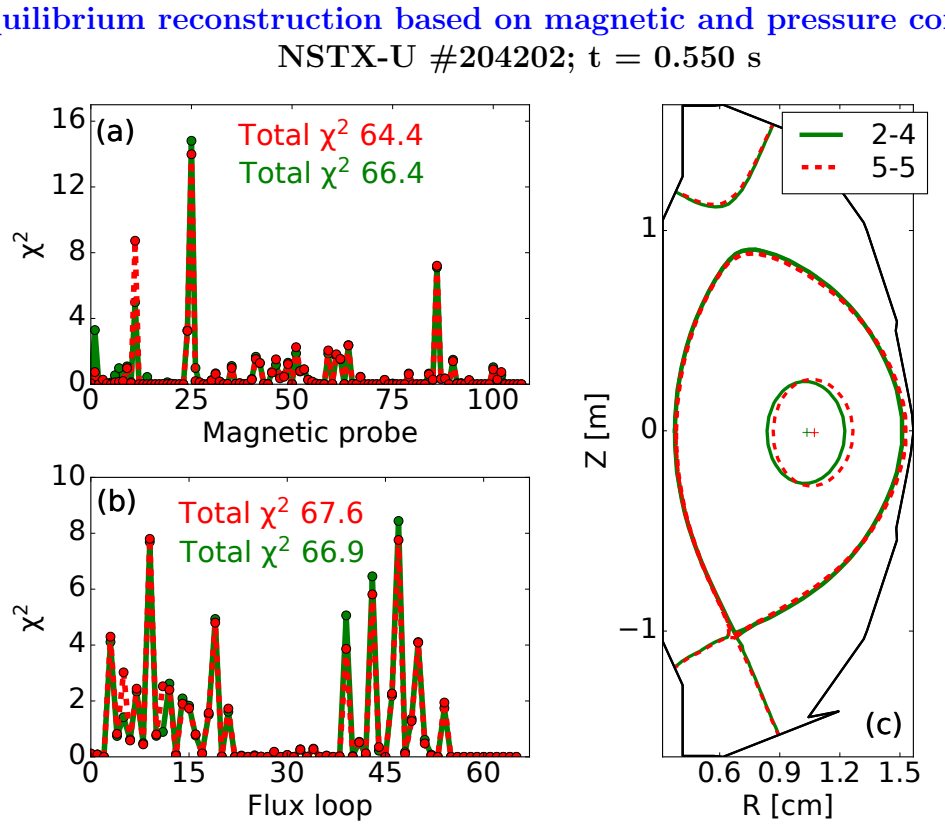

Figure 29. Equilibrium reconstruction based on magnetic and experimental pressure constraints: χ^2 of each magnetic probe (a) and each flux loop(b), magnetic topology of two magnetic equilibria obtained with different polynomial order for pressure (first number) and current (second number) basis functions (c).

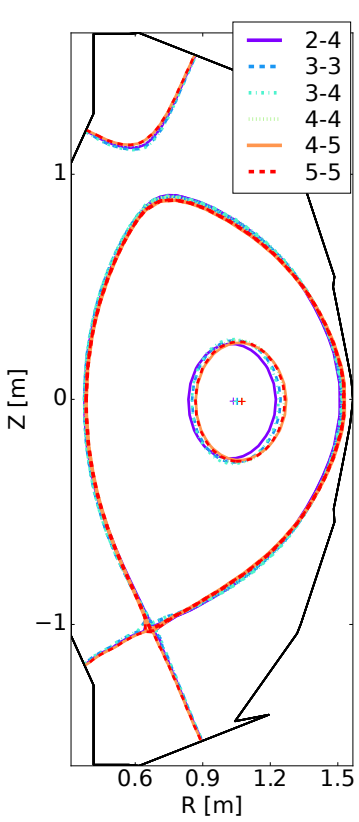

Figure 30. Magnetic topology obtained during variations of the polynomials order for pressure (first number in the legend) and poloidal current (second number in the legend) basis functions.

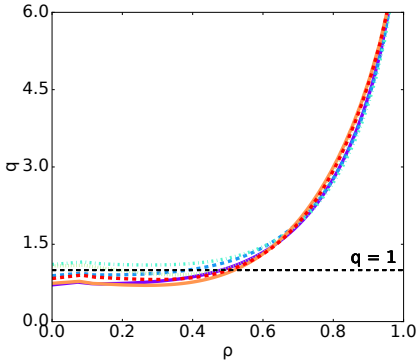

Figure 31. Reconstructed safety factor profiles obtained during variations of polynomials order for pressure (first number in the legend) and poloidal current (second number in the legend) basis functions.

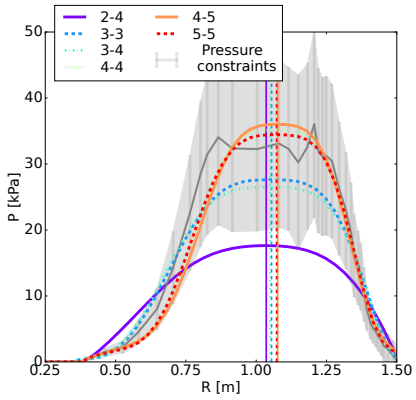

Figure 32. Reconstructed pressure profiles obtained during variations of polynomials order for pressure (first number in the legend) and poloidal current (second number in the legend) basis functions shown together with experimental pressure constraints.

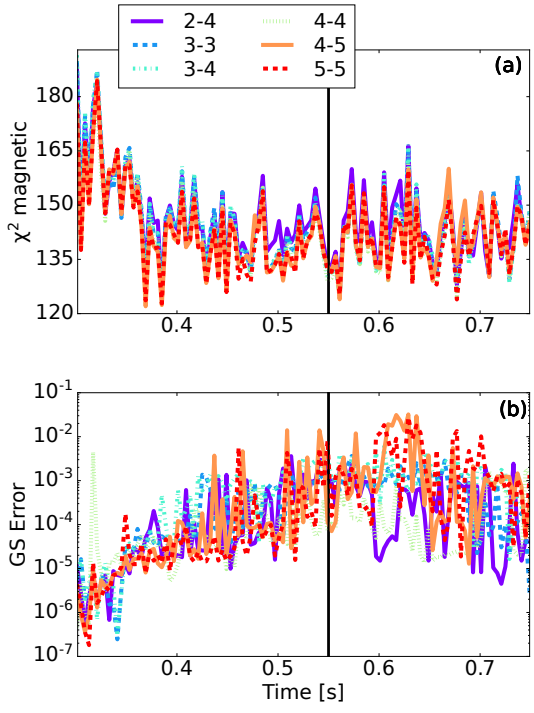

Figure 33. Magnetic χ^2 (a) and GS errors (b)obtained during variations of polynomials order for pressure (first number in the legend) and poloidal current (second number in the legend) basis functions.

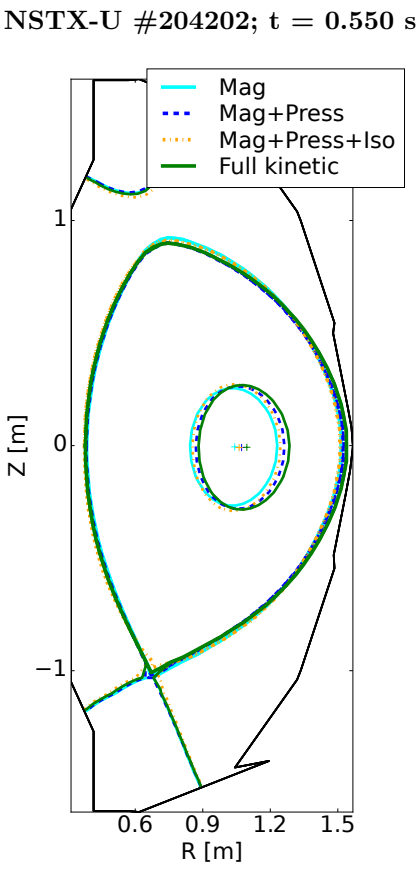

Figure 34. Magnetic topology from reconstructions with various number of constraints.

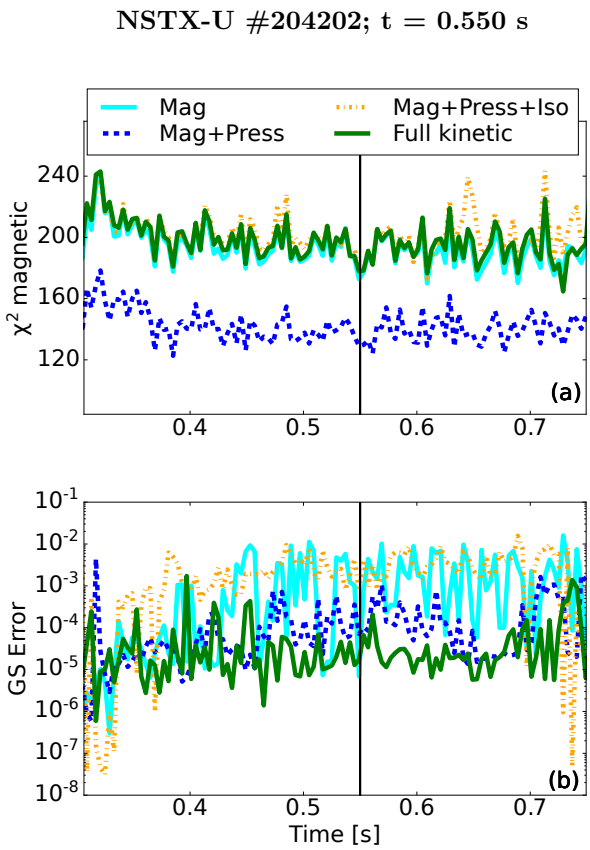

Figure 35. χ^2 error of magnetic diagnostics (a); GS convergence error (b) shown for reconstructions with various number of constraints. A significantly smaller error for *Mag+Press* case is associated with reduced error only for the one probe - # 85 shown on Fig 29.

.

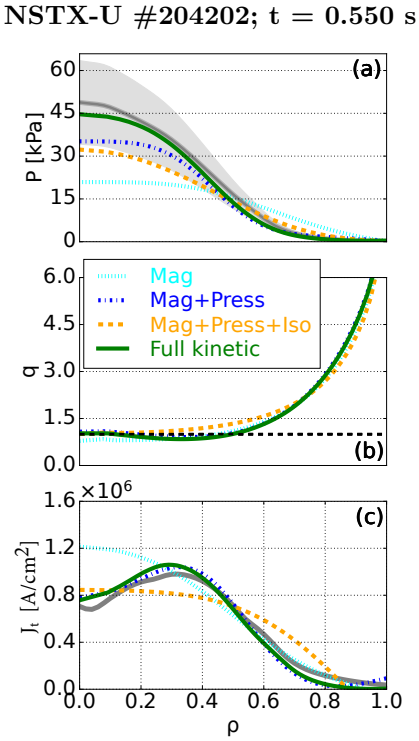

Figure 36. Pressure profile (a), safety factor (b), and current density profiles (c) are plotted over flux coordinates for reconstructions with various number of constraints. Grey curves show pressure and current density profiles obtained from TRANSP simulations. Grey area (a) indicates the uncertainty imposed on the pressure constraints.

6. Conclusion

The equilibrium reconstruction provided by the EFIT code is a solution of the GS equation which satisfies imposed constraints based on the experimental data and transport code simulations. Therefore, the accuracy of the equilibrium depends on the reliability of numerical simulations, quality and amount of available experimental measurements as well as data consistency between all constraints. As the pressure and current density profiles are parameterized in terms of linear basis functions to solve the GS equation, the precision of the equilibrium reconstruction also depends on the representation of basis functions.

The focus of this work is to identify the optimal settings for the kinetic equilibrium reconstruction workflow on NSTX(-U) and estimate a sensitivity of the solution to the polynomial order or the spline tension of basis functions representation. The amount of information about the internal plasma profiles determines the optimal choice of the polynomial representation: to avoid the degeneracies in the solution or provide the accurate detailed fit of the profiles structures. Each step of the workflow conducted through the OMFIT framework is described in detail and demonstrated for selected plasma discharges on NSTX and NSTX-U.

Reconstruction of the NSTX plasma revealed that only external magnetic data is not sufficient to obtain a converged solution of the GS equation if the polynomial order for pressure basis functions is bigger than two. Even if a converged solution is obtained with low polynomial order, the reconstructed total pressure profile is significantly smaller compared to one obtained with experimental measurements and assumptions of unknown fast-ion contribution. In contrast, converged solutions are obtained with various polynomials order of basis functions during NSTX-U reconstruction, demonstrating relatively low sensitivity to the polynomial order variations. This is likely attributed to the larger number of magnetic sensors used to provide equilibrium constraints on NSTX-U compared to NSTX.

Equilibrium reconstructions obtained with magnetic and kinetic pressure constraints based on experimental measurements show that solutions with higher polynomial order demonstrate more peaked pressure profiles, which are closer to experimentally measured kinetic plasma profiles. As expected, the global plasma quantities are determined quite accurately even without strong internal constraints, while other plasma parameters depend on the order of polynomial basis functions. The variations of the magnetic axis and boundary locations can be several centimeters depending on the polynomial order of basis functions. This indicates a large uncertainty of the equilibrium reconstruction based on magnetic and experimental pressure constraints, as different representations of basis functions satisfy the GS solution with the same level of error.

MSE constraints provide constraints on the plasma current at the core region $\rho < 0.7$ and accurate determination of magnetic axis as a location corresponding to the zero pitch angle. A high weight is imposed on these constraints to reach better agreement with experimental measurements across the entire radial domain. In addition, the high weight is required to get a converged solution if both MSE and isothermal constraints are applied during the reconstruction. The latter provides the alignment of LFS and HFS electron temperature and density measurements. With MSE and/or isothermal constraints the solution of the GS equation depends much more weakly on the polynomial order of basis functions. The variations of the magnetic axis and boundary location are reduced to several millimeters and the sensitivity of the safety factor on axis is reduced by a factor of ten.

Changes in the equilibrium reconstruction used for experimental profiles mapping affect the plasma profiles the most in the edge region. Such a dependency is due to strong flux suppression near the LCFS, where even a small shift of the boundary location noticeably affects the mapping of experimental profiles. Meanwhile, a choice of the fitting method more strongly affects the profiles in the core region within $\rho \leq 0.6$. The mapping onto equilibria with various numbers of constraints can result in a 80% change for the electron temperature and up to a 70% change for the electron density in the region $\rho = [0.7 - 1]$. However, within the same radial range, the electron temperature and density profiles are nearly half as sensitive to the choice of the fitting method. The ion temperature and plasma rotation are less sensitive and can vary up to 30% approximately due to changes in the equilibrium and up to 15% due to choice of the fitting method.

According to the transport code simulations, the fast-ion pressure contribution is up to 60% of the total plasma pressure on the axis, and it decreases towards the plasma edge, becoming negligible for $\rho > 0.6$. These calculations are not sensitive to the changes in mapping or fitting of the profiles. However, the equilibrium reconstruction used for the mapping of experimental profiles, as well as the choice of the fitting method affect the current density profile by up to 20% across the entire radial domain. Transport code simulations are validated by various metrics including comparison of calculated signals with experimental measurements.

The solution with transport code constraints has significantly higher gradients at the plasma edge and a close match of pressure constraints at the edge pedestal

region, which are consistent with the kinetic pressure. The consistency of the solution with magnetic and MSE constraints is confirmed by low magnetic χ^2, MSE χ^2, and GS errors for all equilibrium with various number of constraints.

Results of linear CGYRO simulations in the range of low-k modes performed on different types of input data, generated by mapping of experimental data to various types of equilibrium, show that amplitudes of growth rates of unstable modes are different between various cases, which is especially pronounced in the region $k_\theta \rho_s \sim 1$. TGLF simulations show strong dependency on plasma conditions, which results in a discrepancy of predicted fluxes in the range of an order of magnitude. In contrast, the stability analysis performed with the GATO code shows stable plasma conditions to $n = 1$ modes in both the magnetic and kinetic equilibria.

To overall improve the accuracy of the equilibrium reconstruction an increase in diagnostic resolution is required, in particular to decrease the uncertainty and sensitivity of plasma profiles to the choice of the fitting method and mapping in the edge region. Another approach to improve the equilibrium reconstruction is to infer and propagate the uncertainty of the plasma profiles to the transport and equilibrium codes. The impact of rotation constraints is expected to became stronger with an increase of plasma shaping and more quantitative analysis of the impact of rotational constraints on NSTX and NSTX-U plasma is the subject of future work.

The proposed approach can be easily applied to other tokamaks, where some adjustment of the OMFIT workflow might be required based on the configuration of the diagnostic systems as well as available transport codes. One of the main advantage of the proposed method it is an automated coupling of the EFIT code with experimental data analysis tool and transport code simulations, that makes the entire process of the full kinetic equilibrium reconstruction relatively simple and straightforward.

Acknowledgement

This material is based upon work supported by the U.S. Department of Energy, Office of Science, Office of Fusion Energy Sciences under Awards DE-SC0021113 and DE-AC02-09CH11466. This research was supported by the General Atomics Postgraduate Research Participation Program administered by ORAU. Part of the data analysis was performed using the OMFIT integrated modeling framework `http://omfit.io/`. Digital data for this paper can be found in `http://arks.princeton.edu/ark:/88435/dsp018p58pg29j`

References

1. Ongena, J., Evrard, M. & McCune, D. Numerical Transport Codes. *Fusion Technology* **33,** 181–191. ISSN: 0748-1896 (1998).
2. Zohm, H. Assessment of DEMO challenges in technology and physics. *Fusion Engineering and Design* **88,** 428–433. ISSN: 0920-3796 (2013).
3. Tang, W. M. Scientific and computational challenges of the fusion simulation project (FSP). *Journal of Physics: Conference Series* **125,** 012047. ISSN: 1742-6596 (2008).
4. Petty, C. DIII-D research towards establishing the scientific basis for future fusion reactors. *Nuclear Fusion* **59,** 112002. ISSN: 0029-5515 (2019).
5. Luxon, J. & Brown, B. Magnetic analysis of non-circular cross-section tokamaks. *Nuclear Fusion* **22,** 813. `https://dx.doi.org/10.1088/0029-5515/22/6/009` (June 1982).
6. Wesson, J. Tokamaks, 3rd ed. *Clarendon Press* (2004).
7. Lao, L., John, H. S., Stambaugh, R., Kellman, A. & Pfeiffer, W. Reconstruction of current profile parameters and plasma shapes in tokamaks. *Nuclear Fusion* **25,** 1611. `https://dx.doi.org/10.1088/0029-5515/25/11/007` (Nov. 1985).
8. Lao, L. L. *et al.* MHD Equilibrium Reconstruction in the DIII-D Tokamak. *Fusion Science and Technology* **48,** 968–977. `https://doi.org/10.13182/FST48-968` (2005).
9. Xing, Z. *et al.* CAKE: Consistent Automatic Kinetic Equilibrium reconstruction. *Fusion Engineering and Design* **163,** 112163. ISSN: 0920-3796. `https://www.sciencedirect.com/science/article/pii/S0920379620307110` (2021).
10. Menard, J. E. *et al.* Observation of Instability-Induced Current Redistribution in a Spherical-Torus Plasma. *Phys. Rev. Lett.* **97,** 095002. `https://link.aps.org/doi/10.1103/PhysRevLett.97.095002` (9 Aug. 2006).

11. Moret, J.-M. *et al.* Tokamak equilibrium reconstruction code LIUQE and its real time implementation. *Fusion Engineering and Design* **91,** 1–15. ISSN: 0920-3796. https://www.sciencedirect.com/science/article/pii/S0920379614005973 (2015).
12. Faugeras, B. An overview of the numerical methods for tokamak plasma equilibrium computation implemented in the NICE code. *Fusion Engineering and Design* **160,** 112020. ISSN: 0920-3796. https://www.sciencedirect.com/science/article/pii/S0920379620305688 (2020).
13. Lao, L. L. *et al.* Application of machine learning and artificial intelligence to extend EFIT equilibrium reconstruction. *Plasma Physics and Controlled Fusion* **64,** 074001. https://dx.doi.org/10.1088/1361-6587/ac6fff (June 2022).
14. Zakharov, L. E., Foley, E. L., Levinton, F. M. & Yuh, H. Y. Reconstruction of the q and p profiles in ITER from external and internal measurements. *Plasma Physics Reports* **34,** 173–188. ISSN: 1063-780X (2008).
15. Carpanese, F. *et al.* First demonstration of real-time kinetic equilibrium reconstruction on TCV by coupling LIUQE and RAPTOR. *Nuclear Fusion* **60,** 066020. ISSN: 0029-5515 (2020).
16. Berkery, J. W. *et al.* Kinetic equilibrium reconstructions of plasmas in the MAST database and preparation for reconstruction of the first plasmas in MAST upgrade. *Plasma Physics and Controlled Fusion* **63,** 055014. ISSN: 0741-3335 (2021).
17. Rice, B. W., Burrell, K. H., Lao, L. L. & Lin-Liu, Y. R. Direct Measurement of the Radial Electric Field in Tokamak Plasmas using the Stark Effect. *Physical Review Letters* **79,** 2694–2697. ISSN: 0031-9007 (1997).
18. Meneghini, O. *et al.* Integrated modeling applications for tokamak experiments with OMFIT. *Nuclear Fusion* **55,** 083008. ISSN: 0029-5515 (2015).
19. Kaye, S. *et al.* NSTX/NSTX-U theory, modeling and analysis results. *Nuclear Fusion* **59,** 112007. ISSN: 0029-5515 (2019).
20. Menard, J. *et al.* Overview of NSTX Upgrade initial results and modelling highlights. *Nuclear Fusion* **57,** 102006. https://dx.doi.org/10.1088/1741-4326/aa600a (June 2017).
21. Sabbagh, S. *et al.* Equilibrium properties of spherical torus plasmas in NSTX. *Nuclear Fusion* **41,** 1601–1611. ISSN: 0029-5515 (2001).
22. Sabbagh, S. *et al.* Resistive wall stabilized operation in rotating high beta NSTX plasmas. *Nuclear Fusion* **46,** 635. https://dx.doi.org/10.1088/0029-5515/46/5/014 (Apr. 2006).
23. Sabbagh, S. A. *et al.* Beta-limiting instabilities and global mode stabilization in the National Spherical Torus Experiment. *Physics of Plasmas* **9,** 2085–2092. ISSN: 1070-664X. eprint: https://pubs.aip.org/aip/pop/article-pdf/9/5/2085/19228697/2085_1_online.pdf. https://doi.org/10.1063/1.1468230 (May 2002).
24. Breslau, J. *et al. TRANSP is a 1.5D equilibrium and transport solver for interpretation and prediction of tokamak discharges* 2018. https://www.osti.gov/doecode/biblio/12542.
25. NSTX-U Software Home Page. https://nstx.pppl.gov/nstx/Software/index.html.
26. MDSplus introduction. https://www.mdsplus.org/index.php/Introduction.
27. LeBlanc, B. P. & Diallo, A. Alignment of the Thomson scattering diagnostic on NSTX. *Journal of Instrumentation* **8,** C11004–C11004 (2013).
28. LeBlanc, B. P. *et al.* Operation of the NSTX Thomson scattering system. *Review of Scientific Instruments* **74,** 1659–1662. ISSN: 0034-6748. eprint: https://pubs.aip.org/aip/rsi/article-pdf/74/3/1659/19083501/1659_1_online.pdf. https://doi.org/10.1063/1.1532763 (Mar. 2003).
29. Biewer, T. M., Bell, R. E., Feder, R., Johnson, D. W. & Palladino, R. W. Edge rotation and temperature diagnostic on the National Spherical Torus Experiment. *Review of Scientific Instruments* **75,** 650–654. ISSN: 0034-6748 (2004).
30. Jiang, Y. *et al.* Kinetic equilibrium reconstruction and the impact on stability analysis of KSTAR plasmas. *Nuclear Fusion* **61,** 116033. https://dx.doi.org/10.1088/1741-4326/ac26a4 (Oct. 2021).
31. Pankin, A., McCune, D., Andre, R., Bateman, G. & Kritz, A. The tokamak Monte Carlo fast ion module NUBEAM in the National Transport Code Collaboration library. *Computer Physics Communications* **159,** 157–184. ISSN: 0010-4655 (2004).
32. Levinton, F. M. & Yuh, H. The motional Stark effect diagnostic on NSTXa). *Review of Scientific Instruments* **79,** 10F522. ISSN: 0034-6748. eprint: https://pubs.aip.org/aip/rsi/article-pdf/doi/10.1063/1.2968699/15670015/10f522_1_online.pdf. https://doi.org/10.1063/1.2968699 (Oct. 2008).
33. Rice, B., Burrell, K. & Lao, L. Effect of plasma radial electric field on motional Stark effect measurements and equilibrium reconstruction. *Nuclear Fusion* **37,** 517. https://dx.doi.org/10.1088/0029-5515/37/4/I09 (Apr. 1997).

34. Logan, N. C. *et al.* OMFIT Tokamak Profile Data Fitting and Physics Analysis. *Fusion Science and Technology* **74,** 125–134. https://doi.org/10.1080/15361055.2017.1386943 (2018).

35. OMFITprofile tutorial and documentation. https://docs.google.com/document/d/1b3SZtTbBLi6OXycjNozDyUvzc7FZWBLYUDDpvi3plI0/edit#heading=h.nx17l9rfc1dh.

36. Fredrickson, E. D., Bell, M. G., Budny, R. V., Darrow, D. S. & White, R. Anomalous fast ion losses at high on the tokamak fusion test reactor. *Physics of Plasmas* **22,** 032501. ISSN: 1070-664X. eprint: https://pubs.aip.org/aip/pop/article-pdf/doi/10.1063/1.4907656/15902055/032501_1_online.pdf. https://doi.org/10.1063/1.4907656 (Mar. 2015).

37. Gorelenkov, N. N., Fisch, N. J. & Fredrickson, E. On the anomalous fast ion energy diffusion in toroidal plasmas due to cavity modes. *Plasma Physics and Controlled Fusion* **52,** 055014. https://dx.doi.org/10.1088/0741-3335/52/5/055014 (Apr. 2010).

38. Thome, K. *et al.* Response of thermal and fast-ion transport to beam ion population, rotation and Te/Ti in the DIII-D steady state hybrid scenario. *Nuclear Fusion* **61,** 036036. https://dx.doi.org/10.1088/1741-4326/abd862 (Feb. 2021).

39. Baranov, Y. F. *et al.* Anomalous and classical neutral beam fast ion diffusion on JET. *Plasma Physics and Controlled Fusion* **51,** 044004. https://dx.doi.org/10.1088/0741-3335/51/4/044004 (Mar. 2009).

40. Zarnstorff, M. C. *et al.* Parallel electric resistivity in the TFTR tokamak. *Physics of Fluids B: Plasma Physics* **2,** 1852–1857. ISSN: 0899-8221. eprint: https://pubs.aip.org/aip/pfb/article-pdf/2/8/1852/12324101/1852_1_online.pdf. https://doi.org/10.1063/1.859456 (Aug. 1990).

41. Spitzer, L. & Härm, R. Transport Phenomena in a Completely Ionized Gas. *Phys. Rev.* **89,** 977–981. https://link.aps.org/doi/10.1103/PhysRev.89.977 (5 Mar. 1953).

42. Sauter, O., Angioni, C. & Lin-Liu, Y. R. Neoclassical conductivity and bootstrap current formulas for general axisymmetric equilibria and arbitrary collisionality regime. *Physics of Plasmas* **6,** 2834–2839. ISSN: 1070-664X. eprint: https://pubs.aip.org/aip/pop/article-pdf/6/7/2834/19054899/2834_1_online.pdf. https://doi.org/10.1063/1.873240 (July 1999).

43. Houlberg, W. A., Shaing, K. C., Hirshman, S. P. & Zarnstorff, M. C. Bootstrap current and neoclassical transport in tokamaks of arbitrary collisionality and aspect ratio. *Physics of Plasmas* **4,** 3230–3242. ISSN: 1070-664X (1997).

44. Poli, F. M. *et al.* Experimental and modeling uncertainties in the validation of lower hybrid current drive. *Plasma Physics and Controlled Fusion* **58,** 095001. https://dx.doi.org/10.1088/0741-3335/58/9/095001 (July 2016).

45. Zarnstorff, M. C. *et al.* Parallel electric resistivity in the TFTR tokamak. *Physics of Fluids B: Plasma Physics* **2,** 1852–1857. ISSN: 0899-8221. eprint: https://pubs.aip.org/aip/pfb/article-pdf/2/8/1852/12324101/1852_1_online.pdf. https://doi.org/10.1063/1.859456 (Aug. 1990).

46. Candy, J., Belli, E. & Bravenec, R. A high-accuracy Eulerian gyrokinetic solver for collisional plasmas. *Journal of Computational Physics* **324,** 73–93. ISSN: 0021-9991 (2016).

47. Staebler, G. M., Kinsey, J. E. & Waltz, R. E. Gyro-Landau fluid equations for trapped and passing particles. *Physics of Plasmas* **12,** 102508. ISSN: 1070-664X (2005).

48. Avdeeva, G. *et al.* Energy transport analysis of NSTX plasmas with the TGLF turbulent and NEO neoclassical transport models. *Nuclear Fusion* **63,** 126020. https://dx.doi.org/10.1088/1741-4326/acfc56 (Oct. 2023).

49. Berkery, J. W. *et al.* NSTX-U research advancing the physics of spherical tokamaks. *Nuclear Fusion.* http://iopscience.iop.org/article/10.1088/1741-4326/ad3092 (2024).

50. P., B. D. *et al.* Tearing mode stability studies near ideal stability boundaries in DIII-D. *Physics of Plasmas* **9,** 2998–3006. ISSN: 1070-664X. eprint: https://pubs.aip.org/aip/pop/article-pdf/9/7/2998/19222065/2998_1_online.pdf. https://doi.org/10.1063/1.1481504 (July 2002).

51. Turnbull, A. D., Brennan, D. P., Chu, M. S., Lao, L. L. & Snyder, P. B. Theory and Simulation Basis for Magnetohydrodynamic Stability in DIII-D. *Fusion Science and Technology* **48,** 875–905. https://doi.org/10.13182/FST05-A1046 (2005).

52. Bernard, L., Helton, F. & Moore, R. GATO: An MHD stability code for axisymmetric plasmas with internal separatrices. *Computer Physics Communications* **24,** 377–380. ISSN: 0010-4655. https://www.sciencedirect.com/science/article/pii/0010465581901600 (1981).

53. Bateman, G. & Peng, Y. .-. M. Magnetohydrodynamic Stability of Flux-Conserving Tokamak Equilibria. *Phys. Rev. Lett.* **38,** 829–832. https://link.aps.org/doi/10.1103/PhysRevLett.38.829 (15 Apr. 1977).

54. Gerhardt, S. P. *et al.* Magnetic diagnostics for equilibrium reconstruction and realtime plasma control in NSTX-Upgradea). *Review of Scientific Instruments* **85,** 11E807. ISSN: 0034-6748. eprint: https://pubs.aip.org/aip/rsi/article-pdf/doi/10.1063/1.4889781/14064480/11e807_1_online.pdf. https://doi.org/10.1063/1.4889781 (July 2014).